

Fabrication of Optical Microfibers

Masterarbeit in Physik

von
Christian Lützler

angefertigt im Institut für Angewandte Physik,
vorgelegt der Mathematisch-Naturwissenschaftlichen Fakultät
der Universität Bonn
im September 2012

Contents

1. Introduction	1
2. Theory of tapering optical fibers	3
2.1. Features of optical microfibers	3
2.2. From simple tapering to advanced shaping	4
2.3. Flame brushing technique	7
2.3.1. Amplitude of flame brushing	7
2.3.2. Flame trip calculation	11
2.4. Optimum temperature for the deformation of optical fibers	14
2.4.1. Crystallization of fused silica	14
2.4.2. Viscosity of fused silica	14
3. Assembly for the fabrication of OMFs	17
3.1. Overview	17
3.2. Fiber positioning and alignment	19
3.3. Gas burner and fuel supply system	22
3.4. Optical microscope	26
3.5. Control electronics	28
4. Effect of flame heating on the optical fiber	31
5. Analysis of the microfibers	37
5.1. Light transmission	37
5.2. General remarks on the shape analysis of the OMF	39
5.3. Taper profile	42
5.4. Waist diameter	46
5.5. Waist length	49
6. Summary and conclusion	53
7. Outlook	55
7.1. Suggested improvements and extensions	55
7.2. Possible future experiments	56
A. Source code	57
A.1. Source code of the flame brushing amplitude calculation	57
A.2. Calculation of flame trips	60
A.3. Control software for mbed microcontroller	65

B. Parameters of the presented OMFs	71
Bibliography	72
Acknowledgements	75

Erster Gutachter: Prof. Dr. Dieter Meschede
Zweiter Gutachter: Prof. Dr. Stefan Linden

1. Introduction

The use of optical fibers as light waveguides is nowadays a well established technique not only in science [1] but also in telecommunication [2] as well as in medical applications [3]. Optical fibers even make their way to home use in high bandwidth data transmission applications [4]. Especially in optics laboratories the need for optical fibers as light waveguides is high and optical fibers are often more advantageous than free space propagation of light beams.

In particular, so called optical microfibers (OMFs) with diameters on the order of one micrometer have attracted much attention during the last years [5–8]. This results from the optical properties of the OMFs. Due to the small cross section of the OMF about 50% of power guided through it propagates outside the physical boundary of the OMF. The portion of light guided by the fiber but propagating in the surrounding medium is referred to as the evanescent field. This field can be accessed rather easily for experiments and offers high light intensity because of the strong spacial confinement.

A typical application of OMFs is spectroscopy [6, 9], which is the most prominent example for light matter interaction. Further applications are non-linear optics like generation of higher harmonics [10] or the use of OMFs as interferometers in which the two paths are represented by two transverse fiber modes [11]. An ongoing field of research is creating optical traps for ultra cold atoms with the help of a standing light wave inside the OMF [12]. For all the different applications mentioned here the OMF must have suitable properties in terms of geometry and thus light guidance. Additionally, to be able to reproduce experimental data with OMFs their fabrication must be reliable and reproducible, too.

Until now for fabrication of OMFs a setup that has been developed in this research group [13] was used but belongs to the group of Arno Rauschenbeutel [14]. Very recent work reaches the limitations of the current fabrication apparatus [11]. This thesis work lays the foundations for the on-demand fabrication of OMFs of any shape and with various optical properties. The scope of this work covers among others the design of an advanced mechanical setup, the corresponding calculations on fabrication of OMFs, and the analysis and verification of the properties of the resulting OMFs.

2. Theory of tapering optical fibers

2.1. Features of optical microfibers

The term *optical microfiber (OMF)* is one of the common names in use for tapered fused silica optical waveguides. These special optical fibers exhibit a region in which the fiber diameter is significantly lower than the standard diameter of usually $125\ \mu\text{m}$. As the term *microfiber* indicates, the diameters present at these waveguides are typically between a few hundred nanometers only and some micrometers¹. Just a small section with a length of millimeters along the optical fiber is tapered down to the minimum diameter. This section of minimum diameter is denoted as the microfiber *waist*. The waist is connected to the residual fiber of initial diameter via two symmetric transitions² of multiple length of the waist. These transitions are referred to as the *tapers* of the microfiber. The geometry of a typical microfiber is illustrated in Fig. 2.1.

In all step-index optical fibers made from fused silica the light guidance is provided by the difference in refractive index between core and cladding, which results from the core dopant. Due to the small difference in refractive index this level of guidance is called *weak guidance*. The field energy of the fundamental transverse fiber mode (HE_{11}) propagates in the core of the fiber and only hardly extends into the cladding, see Fig. 2.2a. Together with the decrease in diameter from an unprocessed optical fiber to a microfiber goes a remarkable modification of the light guiding properties. At the waist of the microfiber a significant fraction of the light field propagates outside the physical boundary of the fiber, see Fig. 2.2b. The core diameter decreases in the same ratio as the cladding diameter does when tapering the fiber. So the tapered fiber bases on the identical structure as the initial fiber. But the much smaller core diameter is no longer resolved by the light field when traveling through

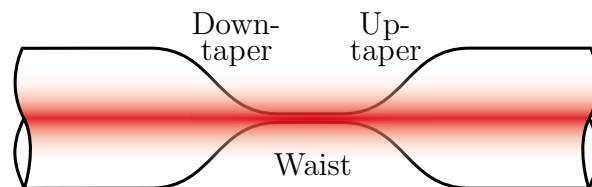


Figure 2.1. Shape of a typical OMF. The initial fiber diameter is connected to the waist section via two symmetric tapers. The drawing is not to scale.

¹The term *OMF* is extended in this thesis to all tapered optical fibers, independent of the exact minimum diameter.

²Asymmetric transitions are possible but not considered in this thesis.

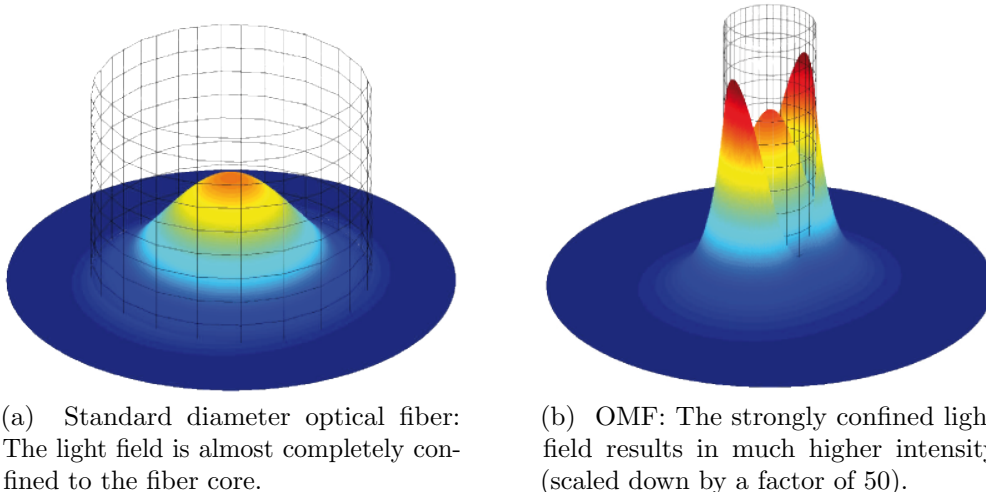


Figure 2.2. Calculated field distributions for the fundamental transverse fiber mode (HE_{11}) for a standard diameter optical fiber (a) and an OMF (b). Taken from [15].

the OMF. As a consequence the weak guidance changes to *strong guidance* by the boundary of fiber cladding and surrounding medium, usually air.

2.2. From simple tapering to advanced shaping

The fabrication of OMFs bases on the conservation of mass. It comes to application when the bare fiber material is locally heated and the viscosity lowers so that it allows deformation. The latter is introduced by a symmetric pulling force. It acts on the fiber ends along their axis and thus causes the fiber diameter to shrink in the hot section. See Fig. 2.3 for the basic principle. Effects of thermal expansion or evaporation of the fused silica can be neglected [16].

For further investigation the fiber is assumed to have a hot zone of constant length L . In this zone the viscosity of the fiber is assumed to be uniform and significantly lower than in the rest of the considered fiber. This reflects the strong temperature dependence of fused silica viscosity.

Let the initial fiber diameter along the hot zone be D_0 . Then the conservation of mass for this section can be expressed as

$$\frac{\pi}{4} D_0^2 L = \frac{\pi}{4} (D_0 + \delta D)^2 \cdot (L + \delta x) \quad (2.1)$$

for the infinitesimal elongation δx and the resulting negative change in fiber diameter δD . Only linear terms are considered after expanding, as valid for an infinitesimal elongation. The resulting differential equation is

$$\frac{dD}{dx} = -\frac{D}{2L}. \quad (2.2)$$

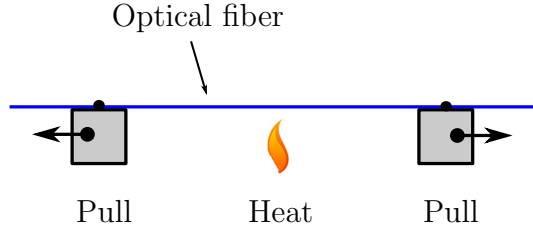


Figure 2.3. Simple tapering of the optical fiber by pulling the ends apart while the fiber material is locally heated by a flame.

With the fiber diameter $D_0 = D(x = 0)$ the integration of this relation yields

$$D(x) = D_0 \cdot \exp\left(-\frac{x}{2L}\right), \quad (2.3)$$

where L is the length of the hot fiber zone.

This idea of simple fiber pulling leads to a very limited variety of possible shapes of OMFs. Any waist diameter can be reached by selecting the fiber elongation x accordingly. But the resulting taper shape is always exponential for a constant hot fiber zone L . This is because with every elementary elongation step the current fiber diameter is pulled out of the hot zone. Therefore, according to Eq. 2.3, an exponential taper is obtained. Consequently, in the approach of simple fiber pulling either the length of the waist or that of the taper can be considered as a degree of freedom. The length of the OMF waist equals the length of the hot fiber zone. Once the final elongation is reached, the hot zone is the only section of constant diameter.³

These relations are illustrated in Fig. 2.4. It shows the simulated profiles of two OMFs obtained with different hot zone lengths ($L = 2\text{ mm}$ and $L = 7\text{ mm}$). The waist diameter for both OMFs is $0.5\ \mu\text{m}$. The blue profile results from $L = 7\text{ mm}$. It has the longer waist and the shallower tapers. With $L = 2\text{ mm}$ a shorter waist and steeper tapers are obtained.

The fiber tapers have a crucial role concerning the light guidance through the OMF. This is because the taper angle⁴ determines the coupling between different transverse fiber modes. Detailed calculations are for example provided in [17] and [11]. As a summary, the shallower the taper the more adiabatic the light is coupled from core-guidance at the initial diameter to cladding-guidance at the OMF waist. The transition can happen almost without decrease in light transmission when the taper angle is as low as a few milliradians [17]. Therefore, it is a crucial prerequisite to be able to control the taper angle precisely for all OMFs. In particular, for applications of OMFs as modal interferometers the coupling of the single incident mode to two or

³The fact that the same fiber diameter is obtained for the entire hot fiber zone can nicely be seen in the analogy of a mechanical spring instead of the hot zone of the optical fiber. The fiber's viscosity translates into the spring constant. When the ends are moved apart the obtained elongation distributes over the entire spring equally.

⁴Throughout this work the taper angle is referred to as the angle from fiber edge to fiber axis. This is half of the opening angle of the cone which is represented by the taper section of the optical fiber.

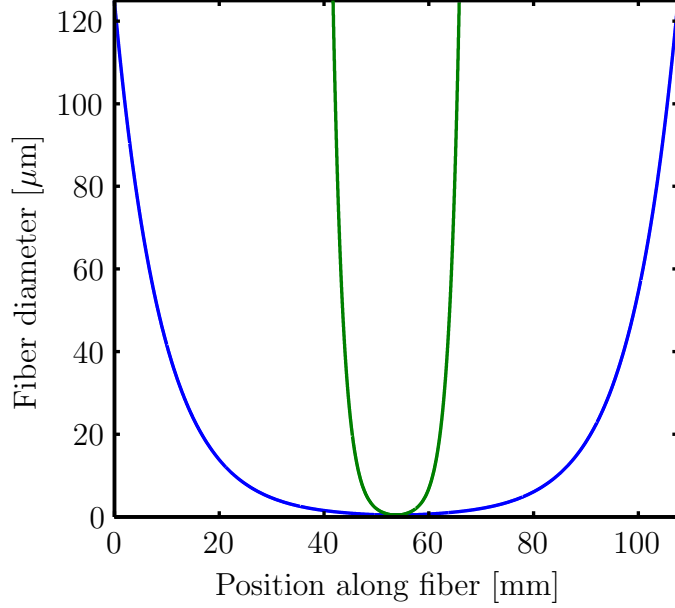


Figure 2.4. Two profiles of OMFs fabricated with different constant hot zone sizes. The shallow tapers (blue) are obtained with the hot zone size of 7 mm, the steep tapers (green) result from 2 mm hot zone size. The lengths of the waists scale correspondingly.

more modes is controlled via the taper angle [11]. This is why a more sophisticated OMF fabrication routine than simple pulling is needed.

The basic ideas on fabrication of arbitrarily shaped OMFs have been published by BIRKS and LI [16]. The underlying principle is to change the length of the hot fiber section throughout the pulling process, i.e. $L \equiv L(x)$. Accordingly, the modification of equation (2.3) reads as

$$D(x) = D_0 \cdot \exp\left(-\frac{1}{2} \int_0^x \frac{dx'}{L(x')}\right). \quad (2.4)$$

This is the basis of all computations concerning the OMF shape. One finds that with an appropriately decreasing hot zone the tapers of the OMF approach the linear shape. Once linear tapers can be fabricated, any shape can be approximated by sections of linear slopes. The length of the OMF waist can be determined by changing the hot zone size for the last step of fiber elongation correspondingly.

The variation in length of the hot fiber zone with fiber elongation can be implemented by having a sufficiently small flame traveling quickly⁵ and bidirectionally along the fiber axis, and considering the amplitude of that oscillating motion to be fiber elongation-dependent. This fabrication technique proves to work in many applications. It is often referred to as the *flame brushing technique* because this term visualizes the procedure [18, 19].

⁵The flame is quickly traveling in comparison to the rate of elongation of the fiber. Typically the fiber is elongated by 100 $\mu\text{m/s}$. So for the flame brushing velocities as low as millimeters per second are sufficient.

Instead of the flame also the fiber can move bidirectionally. This approach corresponds to a change in coordinate frame so that the flame is at rest. The microfiber fabrication setup presented in this work bases on this idea. One advantage is that there is no need to move a flame which is challenging from the point of fuel supply.

2.3. Flame brushing technique

To fabricate OMFs with the flame brushing technique it turns out that there are two calculations required. The first determines which amplitude $L(x)$ the flame brushing oscillation must have throughout the fiber pulling process. The second is on controlling the actual flame trips within the obtained amplitude. For that various parameters come into play: for example, how often the flame brushes the fiber and at which velocity this happens. The two parts of the calculation are presented in the following.

2.3.1. Amplitude of flame brushing

The flame brushing amplitude $L(x)$ is the key to shape the OMF according to a user-defined diameter profile $D(z)$. The considerations published in [16] are applied often when fabricating OMFs [13, 20]. Following these considerations I developed a computation script based on the numerical computing environment `MATLAB`. This script calculates the flame brushing amplitude for any given fiber profile $D(z)$ in three steps. The calculations include a scaling factor which allows choosing between quick but approximative results or precise but more time-consuming calculations. The different levels of computation accuracy are implemented by setting the elementary coordinate and elementary fiber elongation step to large or small values.⁶

The subsequent steps of calculation are sketched. For a deeper understanding I refer to the source code in appendix A.1 in combination with [16]. The coordinates considered here are along the fiber axis z . The zero point is assigned to the transition from the initial fiber diameter to the down-taper.

- **User-given initial values**

The desired geometry of the OMF is required. This covers the final waist diameter, the length of the waist section and the taper profile. The taper profile is specified as a function of coordinate along the ready pulled fiber. Thus, in principle any taper shape is possible. Moreover, the desired computation accuracy has to be defined, too. For typical values see Table 2.1.

The taper length z_0 is obtained from the intersection of the taper profile function and the desired waist diameter. The length of the taper corresponds

⁶The typical total computation time for an entire flame brushing procedure at micrometer accuracy is on the orders of minutes on a modern office computer. But for faster progress during code development the need to perform the entire calculation within seconds arose.

to the coordinate of the transition from taper to waist. This is because of the special choice of the zero point of the coordinate axis. So during the following calculation the instantaneous taper length can be referred to as if it was a coordinate.

- **Step 1**

The first step of computation uses Eq. (2.2) and the geometric relation

$$2z + L(x) = x + L(x = 0). \quad (2.5)$$

This relation can be derived from Fig. 2.5 which compares distances along the fiber from before and during the pulling progress. It connects any position z along the fiber taper to the current elongation x at which this particular point has been pulled out of the hot zone.

A combination of different representations and derivatives of the two mentioned relations and the initial values $D(z)$ and D_w are used for the actual calculation. It leads to the knowledge of the instantaneous length of the hot fiber zone when each point of the taper was pulled out of it, so $L(z)$ is known. The taper-coordinate dependence of the hot zone length is plotted in Fig. 2.6a.

- **Step 2**

Next, the transformation

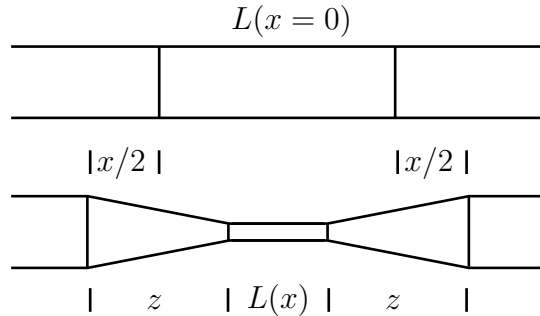
$$x(z) = 2z + L(z) - L(z = 0) \quad (2.6)$$

of Eq. (2.5) is numerically inverted. Using $L(z)$ from step 1 with Eq. 2.6, one obtains the current fiber elongation when any point along the taper was shaped.

Table 2.1. Typical set of user-given properties of an OMF to have the corresponding flame brushing amplitude calculated.

Parameter	Value
D_0	$125 \mu\text{m}$
D_w	$0.5 \mu\text{m}$
L_w	5mm
$D(z)$	$D_0 - 0.003 \cdot z$
Step size	$1 \mu\text{m}$

Figure 2.5. Illustration of Eq. (2.5). The comparison of the unprocessed fiber with the OMF reveals that the initial length of the hot fiber zone together with the total elongation just equals the sum of the length of the tapers and the waist of the OMF.



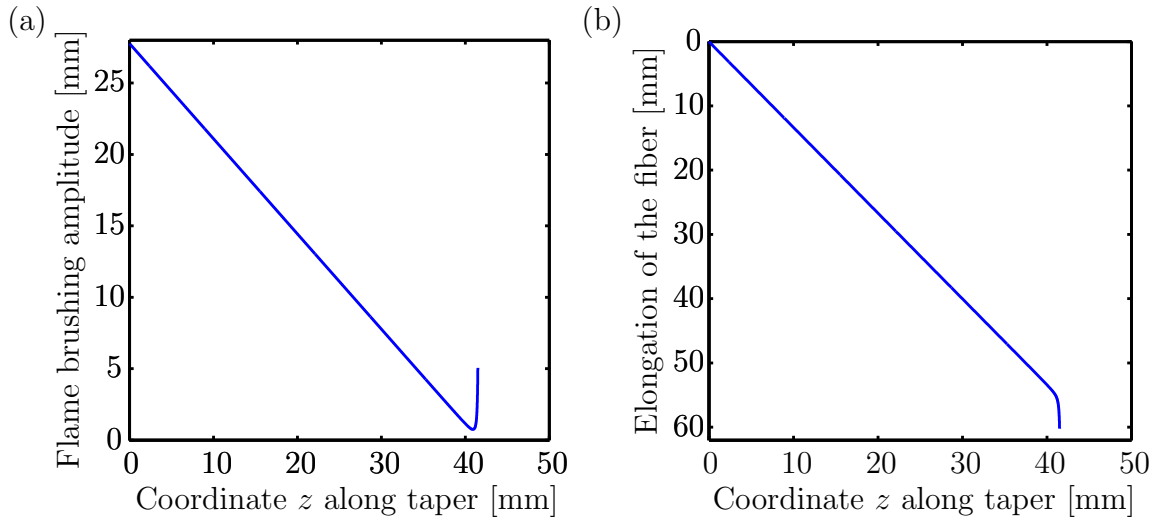


Figure 2.6. Intermediate results of the calculation steps: (a) evolution of the hot zone length parametrized by the taper coordinate, (b) link between the coordinates along the taper and the current elongation of the fiber when the coordinates were pulled out of the hot zone. In both plots the change in slope around $z = 41$ mm reflects the requirement on the hot zone length to equal the length of the waist of the OMF (here: $L_w = 5$ mm) at the final step of elongation.

The resulting connection between the positions z along the taper and the corresponding stage of fiber elongation $x(z)$ is plotted in Fig. 2.6b. The fiber elongation has no intrinsic time dependence but for an intuitive understanding it can be assumed to increase linearly with time.

- **Step 3**

The final computation stage combines the results of the two previous steps. Another transformation of Eq. (2.5) relates $L(z)$ to $x(z)$. This yields the desired hot zone length in dependence of the fiber elongation, $L(x)$. This is the evolution of the flame brushing amplitude during the pulling progress. The result is illustrated in Fig. 2.7.

The result of the calculations (Fig. 2.7) nicely shows that a decreasing hot zone length leads to linear tapers. One can see that when the calculation comes to the very last section of the taper, the hot zone length increases again and reaches the value of exactly 5 mm. This hot zone length corresponds to the desired length of the waist of the OMF fabricated in this particular case.

BIRKS and LI [16] showed how to obtain the shape of the OMF from a given hot zone variation $L(x)$, too. This, however, must not be confused with the simulation of the flame brushing technique. It is only the reversed calculation starting with $L(x)$ and leading to the fiber profile $D(z)$. I implemented this method to have a verification of the computed hot zone length, which results from the three previous steps of calculation. In Fig. 2.8 the comparison of computation step sizes can be seen. The largest deviation between the simulated and the desired fiber shape occurs

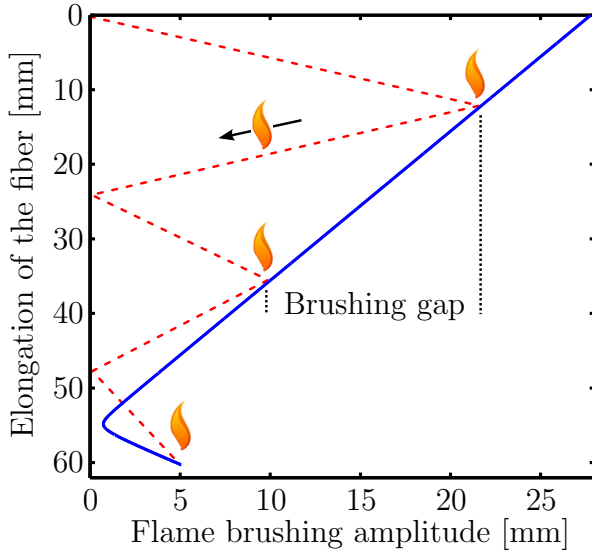


Figure 2.7. Calculated amplitude of the flame brushing motion during the OMF fabrication process. It combines the decrease and increase in size of the hot fiber zone and thus allows arbitrary combinations of taper and waist geometries. A symbolic brushing motion (red dotted line) is included. One clearly sees that the number of brushing trips (here: five) must match the calculated amplitude and the gap at the turnings need to fit to the actual flame size.

at the very end of the fabrication process. This is when the flame brushing amplitude changes rapidly to match the desired waist length. For a computation step size of $10\ \mu\text{m}$ along the fiber axis the largest relative deviation is below $3 \times 10^{-2}\%$. This is suitable for most OMFs. The deviation is two orders of magnitude smaller for a step size of $1\ \mu\text{m}$. These deviations probably arise because I used numerical methods for the inversion and integration of functions. One would expect that these methods yield more accurate results for smaller step sizes, which is indeed observed here. Besides, these calculation inaccuracies occur both at the calculation of $L(x)$ and at the vice-versa calculation for $D(z)$. So the effect on $L(x)$ is probably even less than what is seen in Fig. 2.8.

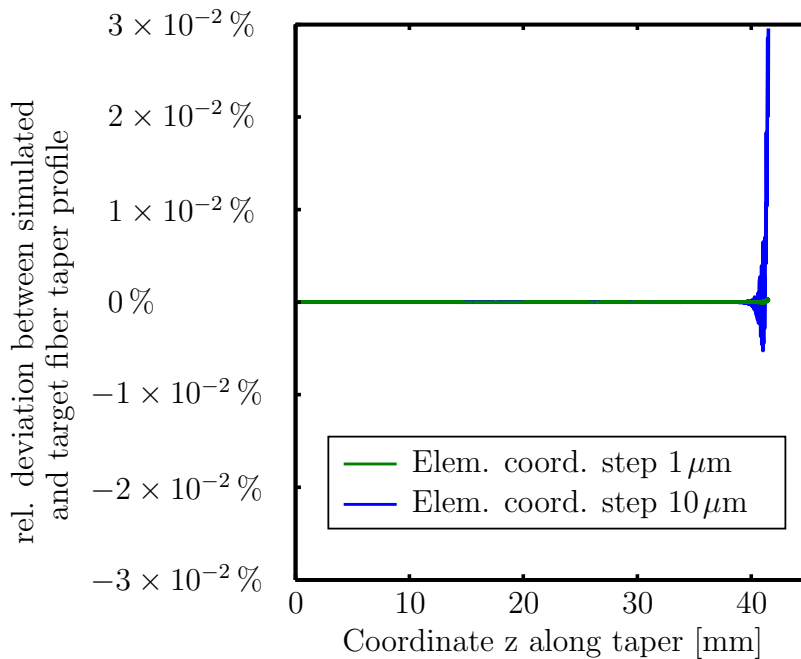


Figure 2.8. Relative deviation between simulated fiber taper profile from the hot zone size and the desired profile for two different elementary coordinate steps.

2.3.2. Flame trip calculation

The computed amplitude of the flame brushing $L(x)$ serves as the basis for the next sequence of calculations. In this section I first have to introduce additional parameters, which are not covered by the computation of $L(x)$. The influence of these parameters is discussed and approximate values are given. Afterwards, the flame brushing motion can be obtained. In a final step the dependence on fiber elongation is translated into time dependence so that usual motion commands are obtained, which relate time and space.

Additional parameters for the flame brushing procedure

The first two parameters are

- a) the number of flame brushing trips
- b) the size of the brushing gap at the turning points of flame motion.

These two parameters are illustrated in Fig. 2.7. The red, dashed line shows a symbolic flame brushing motion. It is the extreme case of only five brushing trips. The larger the number of brushing trips the smaller becomes the brushing gap. The optimum combination of these parameters has to be found experimentally. But it is required that during each flame trip the fiber elongation is constant.

The number of flame brushing trips must be large enough so that all features of the brushing amplitude are sufficiently well resolved. However, the corresponding brushing gap must match the extension of the flame in use. A too small gap causes flame overlap and post-elongates the taper section from the previous flame trip. A too large gap creates fiber sections, which are not completely processed. Both cases can lead to unintended steps along the fiber taper.

For the further calculations the number of flame trips is assumed to be fixed and this indirectly fixes the brushing overlap. The experiments show that for fiber taper angles of a few milliradians approximately one flame brushing trip per millimeter along the taper is a good choice. Typically, up to 90 flame brushing trips can be needed for the fabrication of an OMF.

The used algorithm, which bases on the conservation of mass, is not strictly time-dependent. The time dependence has to be introduced when it comes to the actual motion commands for the OMF fabrication procedure. Therefore, another two parameters have to be introduced:

- c) the elongation rate of the fiber
- d) the speed of flame movement

Just as the parameters a) and b) these two are closely linked, too. Let the fiber elongation rate be given. Then the duration of the OMF fabrication is determined

by the total elongation required. The duration of each flame trip equals the total duration divided by the fixed number of flame trips. Consequently, the speed of flame movement is fixed indirectly. When a specific speed is required, it can be implemented by choosing the fiber elongation rate accordingly.

The typical fiber elongation rate is round $100\ \mu\text{m/s}$. The corresponding flame move velocity is approximately $2.5\ \text{mm/s}$ averaged over an entire trip (including acceleration and deceleration). Experiments show that the peak velocity should not exceed approximately $4\ \text{mm/s}$ because of the heating time constant of the optical fiber.

Flame brushing motion as a function of fiber elongation

The subsequent calculations of the flame brushing motion are again structured into three steps. The full source code is provided in appendix A.2.

- **Step 1**

The instantaneous hot zone length – as obtained from the previous calculations (see Fig. 2.7) – is symmetrically distributed around the center. As a result both the lower and the upper flame brushing limits become dynamic. This corresponds to the application of a symmetric pulling force.

- **Step 2**

Next, the total fiber elongation required is divided by the number of brushing trips. This fulfills the requirement of constant fiber elongation per flame trip. As a side effect it ensures that at the end of the fiber pulling process the flame has just completed an integer number of trips.

- **Step 3**

The actual moves of the flame are now calculated, see Fig. 2.9 for the result. To obtain the bidirectional moves for the flame the dynamic flame limits (from step 1) and the fiber elongation per trip (from step 2) are combined. The first flame trip starts at the lower limit. The end of the trip is the upper limit at that point when the (constant) elongation for one trip is reached. The resulting distance is the length of the first flame brushing trip. That distance is subsequently divided by the elongation for one trip so that one obtains the elementary flame move per fiber elongation step. With the elementary flame move it is straight forward to assemble the flame moves such that the flame positions during the entire trip are obtained as a function of fiber elongation. For the next brushing trip the direction of movement is reversed and the new elementary flame move is obtained in just the same manner but with the lower and upper limits exchanged. The process repeats until the required fiber elongation is reached.

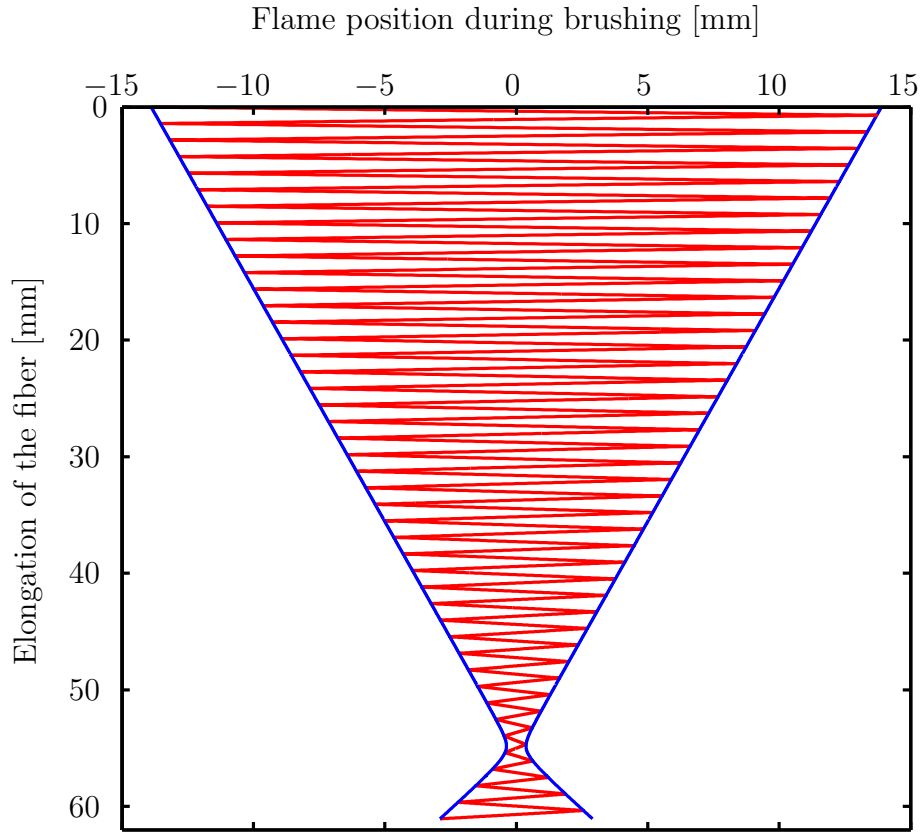


Figure 2.9. 86 flame moves (red oscillation) as a function of fiber elongation are performed within the brushing limits (blue lines). This flame brushing motion corresponds to the OMF geometry from Table 2.1.

Flame brushing motion as a function of time

From the flame brushing motion, parametrized by the fiber elongation, the time-dependent flame moves can be obtained. This step uses the specified elongation rate of the fiber (parameter c). The turning points of the flame brushing motion are used to specify points in space which have to be reached one after another. The constant time period per trip results from the product of the elongation rate and the fiber elongation per flame trip.

As introduced at the end of section 2.2, both the fiber elongation and the flame brushing motion is implemented in the OMF fabrication setup by moving the fiber ends only. Consequently, the obtained flame brushing motion cannot be converted directly into the final motion commands for the setup. The motion commands have to include the fiber elongation. Therefore, the positions extracted from the brushing turning points have to be modified: half of the instantaneous fiber elongation must be added or subtracted, respectively. This results in time-dependent motion commands for the fabrication setup, which include both flame brushing and fiber elongation of the optical fiber. The script, which performs the calculations, writes these movement commands to a data file. The file can be executed to have the OMF fabrication performed under computer control.

2.4. Optimum temperature for the deformation of optical fibers

The fabrication of OMFs bases on the intuitive picture of a flame which locally decreases the viscosity of the fused silica optical fiber. However, the fiber temperature must be within a certain range. On the one hand, a too low fiber temperature does not decrease the material's viscosity enough. On the other hand, a too high fused silica temperature can irreparably lower the light transmission of the optical fiber. This is because of a possible phase transition of SiO_2 . In the following two subsections the lower and the upper temperature limits are derived.

2.4.1. Crystallization of fused silica

Fused silica is the under-cooled melt of SiO_2 . Therefore, at room temperature there are various crystalline states which are energetically more favorable [21]. These are among others α -quartz and β -quartz, which denote different possible crystal structures of SiO_2 . The α -quartz crystal is the only stable form at standard conditions for temperature and pressure [22]. No transition from fused silica to any crystalline state takes place because the transition goes together with the breaking and formation of chemical bonds. This process requires a rather high activation energy. Hence, it is strongly suppressed at room temperature. This is why the under-cooled melt is stable for all practical considerations [21].

This situation changes when the fused silica is heated beyond a temperature of $T_\beta = 1550^\circ\text{C}$. This exact temperature corresponds to the melting point of the β -quartz crystal. When cooling down the optical fiber after heating beyond T_β , β -quartz forms from the hot SiO_2 [21]. The resulting crystals lower the transmittance of the optical fiber⁷ [23]. Therefore, the temperature of the optical fiber must be below $T_\beta = 1550^\circ\text{C}$ when processing it.

When β -quartz crystals have been created in the optical fiber one could expect increased light transmission while heating the fiber just beyond T_β . But β -quartz can transform into energetically favorable derivatives with higher melting points. Consequently, a higher temperature of up to 1705°C would be required to restore the entire initial light transmission of the optical fiber. See [21] for details.

2.4.2. Viscosity of fused silica

In its typical state at room temperature it is difficult to distinguish fused silica from actual solid matter. This is because below temperatures of a few hundred degree

⁷In particular with the flame brushing technique even small losses resulting from hardly exceeding the melting temperature with every flame trip would add up when multiple brushing trips are performed.

Celsius the material's viscosity of $\eta \geq 10^{20} \text{ Pa} \cdot \text{s}$ is much too high to allow inelastic deformation. Thus, for shaping the fiber its viscosity must be lowered. At the so-called annealing point of $\eta = 10^{12} \text{ Pa} \cdot \text{s}$ internal stresses in the glass are released within minutes already. For a bulk of fused silica to deform under its own weight the softening point at $\eta = 10^{6.65} \text{ Pa} \cdot \text{s}$ must be reached [24].

For the fabrication of OMFs from standard optical fiber the material must be deformable but not sag under its own weight. So the viscosity must be above the softening point. But to allow deformation it must be well below the annealing point. According to the considerations on crystallization the maximum fiber temperature is $T_\beta = 1550^\circ\text{C}$. It can be deduced from the plot in Fig. 2.10 that this temperature corresponds to the fused silica viscosity of $\eta \approx 10^{7.8} \text{ Pa} \cdot \text{s}$. This value is between softening and annealing point. So deformation of the optical fiber without loss of light transmission is possible.

For the lower temperature limit the temperature dependence of fused silica has to be investigated. It is strictly monotonically, so a lower fiber temperature always results in a higher viscosity and vice versa. But the precise connection is highly non-linear: As a rough estimation for the considered temperature range the following holds true:

$$\log \eta \propto \frac{1}{T} \quad (2.7)$$

which is a simplification extracted from the empirically found Vogel-Fulcher-Tammann equation [24].

When the fiber temperature decreases from $T_\beta = 1550^\circ\text{C}$ by only 15% the fiber viscosity reaches the annealing point. Consequently, the target temperature for the fabrication of OMFs is just below T_β to allow deformation of the optical fiber at the smallest possible pulling force.

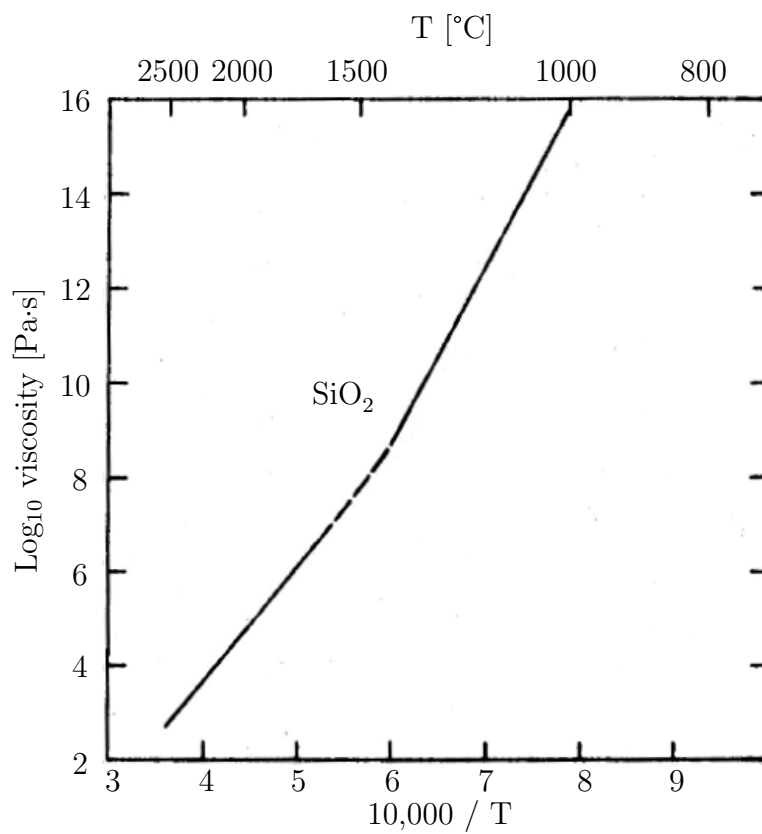


Figure 2.10. Variation of logarithm of viscosity vs. temperature of fused silica (SiO₂). After [24].

3. Assembly for the fabrication of OMFs

3.1. Overview

In this setup the optical fiber moves relative to a stationary gas flame while the elongation takes place. So precise lateral and transverse positioning is required for the fiber ends relative to each other and to the flame. Moreover, a high reproducibility of the OMFs is desired, and the setup must be capable of being extended. Fig. 3.1 shows the optical table with the OMF fabrication assembly on top. I included an enclosure with sliding doors and a flow box because a dust-free environment is essential when processing optical fibers.

For high accuracy alignment and motion a very firm base is required. This is why all parts for positioning the optical fiber are mounted on a granite plate. This granite plate is specified to have a surface flatness better than $3.5\mu\text{m}$. Therefore, differences in height between the individual parts are at maximum of the same value. The granite plate is separated by a $250\mu\text{m}$ thick sheet of PTFE (Polytetrafluoroethylene) from the optical table. Because of its material properties PTFE can “flow” and thus compensate for potential unevenness of the optical table. The granite plate is bordered with clamps which are attached to the optical table. So the two objects form one unit from the mechanical point of view. This combination of the two parts has a significantly higher weight and correspondingly higher inertia compared to the granite plate only. Consequently, any mechanical excitation of the system is strongly suppressed.

The granite plate with the main components of the OMF fabrication setup on top can be seen in Fig. 3.2. There are two motorized translation stages (a). To their top surface the fiber fixation mechanisms are attached (b). This allows positioning of the optical fiber relative to the stationary gas burner (c). Moreover, the setup includes an optical microscope together with a CCD camera (d). This microscope serves the verification of the OMF alignment and the measurement of the OMF diameter.

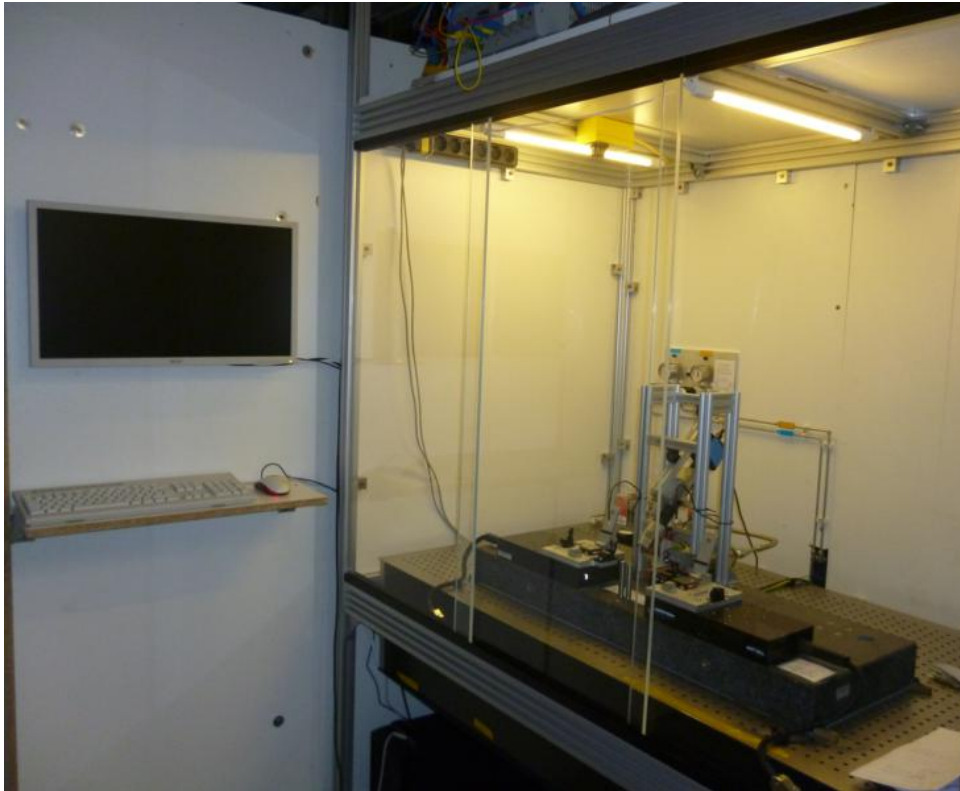


Figure 3.1. Overview of the OMF fabrication assembly. The enclosure ensures a dust-free environment. The control computer is situated next to the fabrication facility.

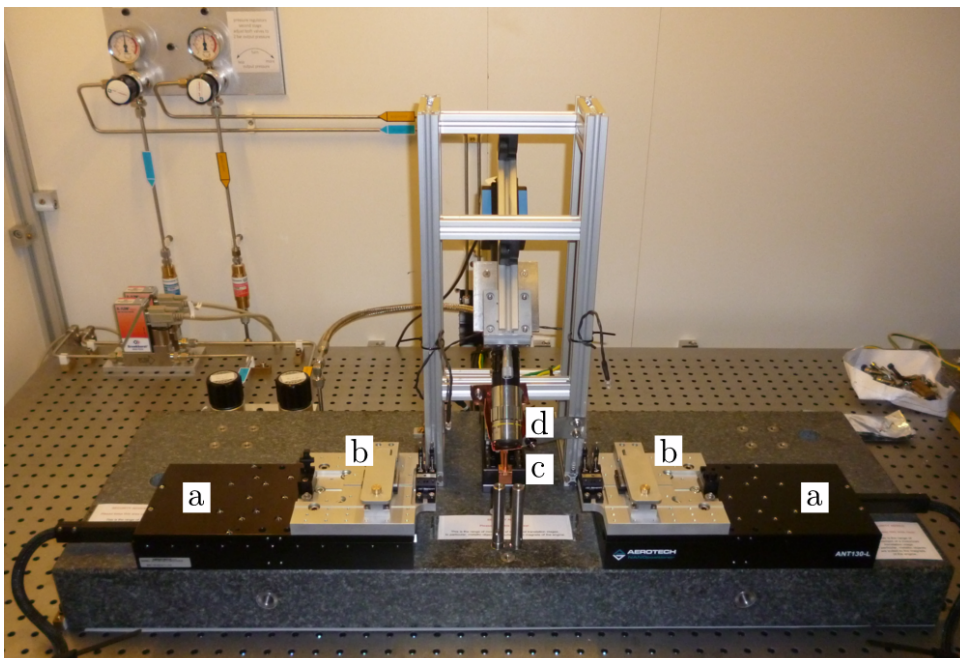


Figure 3.2. Mounting plate of the OMF fabrication assembly made from granite. On top the high accuracy translation stages (a) and fiber fixation platforms (b) are aligned. Moreover, the gas burner (c) and the microscope (d) can be seen. On the back wall of the enclosure there are parts of the gas supply system.

3.2. Fiber positioning and alignment

The combination of the motorized translation stages and the fiber fixation mechanisms is introduced. The features of these components are presented and differences to the previously used setup are discussed.

The two translation stages for this assembly are of the type ANT130-160-L-PLUS from the manufacturer **Aerotech**. That model features a linear motor for almost hysteresis-free, and smooth positioning at a rated step size of only 1 nm. The total positioning accuracy is specified to $\pm 0.3 \mu\text{m}$, including any effects of hysteresis [25]. During operation the observed accuracy is approximately one order of magnitude better. This is because motion velocities much below the rated maximum are used. These particular translation stages go together with analogue current amplifiers to reduce jitter of the motion as much as possible. Some amplifiers for these applications use pulse width modulation which may add jitter to the motion of the translation stage.

The powerful software suite provided by **Aerotech** includes an iterative self-learning algorithm. This piece of software allows in principle for any deviation from the set-movement to be compensated. It is done by repeating a sequence of motion and feeding the errors forward to the system. This allows to take into account position-dependent friction or effects of inertia during acceleration or deceleration. In addition to this the software allows recording the performed moves at the encoder's position resolution of 1 nm. This can help to investigate sources of inaccuracies. Fig. 3.3 shows a typical set of data obtained in this manner, it is a part of the bidirectional flame brushing motion.

The fiber fixation mechanisms on each translation stage must provide a strong clamping force. The strong force is needed to prevent the optical fiber from slipping when the translation stages apply the pulling force. Yet the fixation must be very accurate and reliable. Therefore, I decided to use a fiber fixation which bases only on clamps so that the exact fixation force and position are defined by design. The design guidelines are to have no off-center loads acting on the translation stages and to keep the fiber position as low as possible to maximize the pulling straightness. This makes sure that the torque applied to the bearings of the translation stages is as low as possible with a given fiber pulling force.

For each end of the optical fiber there is a combination of three clamps mounted to a versatile platform (see Fig. 3.4). The platform was milled from a block of stress relieved aluminum so that it does not buckle during or after fabrication. This helps to increase the alignment accuracy of the individual clamps on top of the platform. There is a dedicated clamp (type 466A-710 from **Newport**, a) for precise transverse positioning of the optical fiber. It is the clamp closest to the gas flame because that is where accurate positioning is required. Next to it there is a clamp fabricated from the institute's workshop (b). I designed it to have a long lever so that it can provide the strong fixation force for the optical fiber. The fiber is clamped to a commercial fiber alignment V-groove (type HFM001 from **Thorlabs**) for $D_0 = 125 \mu\text{m}$ fibers. The

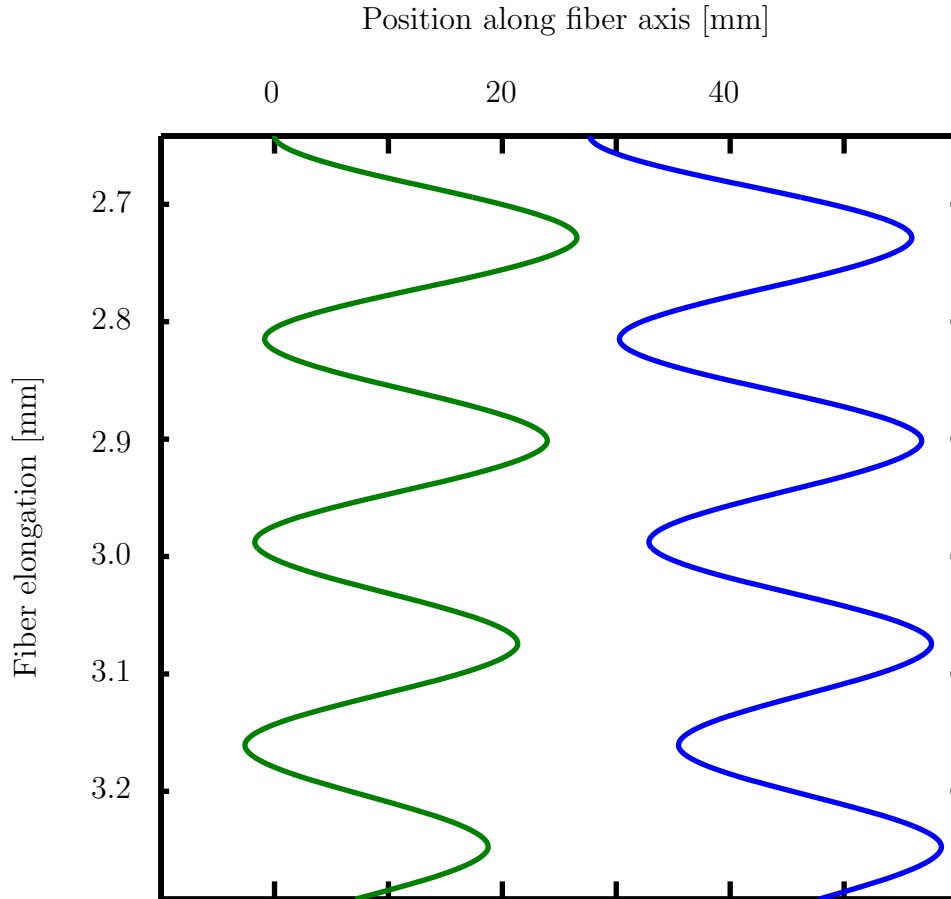


Figure 3.3. Typical motion of the translation stages during fabrication of an OMF (truncated). The two lines correspond to the two translation stages which perform the flame brushing (synchronous oscillation) while elongating the optical fiber (increasing distance). The amplitude of the oscillations decreases so that a linear fiber taper is obtained (compare Fig. 2.9).

third fiber clamp on the platform (type 466A-711 from Newport, c) serves the coarse alignment of the fiber: the stripped and carefully cleaned optical fiber can easily be fixed preliminarily with this clamp to prevent it from being polluted while carefully closing the other clamps one after another.

I carried out both the alignment of the platforms on the translation stages and the alignment of the individual clamps on the platforms with the help of the microscope, which is included in the OMF fabrication assembly (see Fig. 3.12a for a typical microscope image from this procedure). All six V-grooves for the fiber alignment have a maximum transverse positioning error of below $10\mu\text{m}$.⁸ This transverse offset translates into an angular positioning inaccuracy of below 0.1mrad when one considers the distance of approximately 100mm between the two fiber fixation

⁸It is to be said that it is an unexpected challenge for the unexperienced student to screw parts to position with micrometer accuracy. Touching the screw with the screwdriver already leads to deviations from the target position, not to mention any effects of the applied force when tightening the screw.

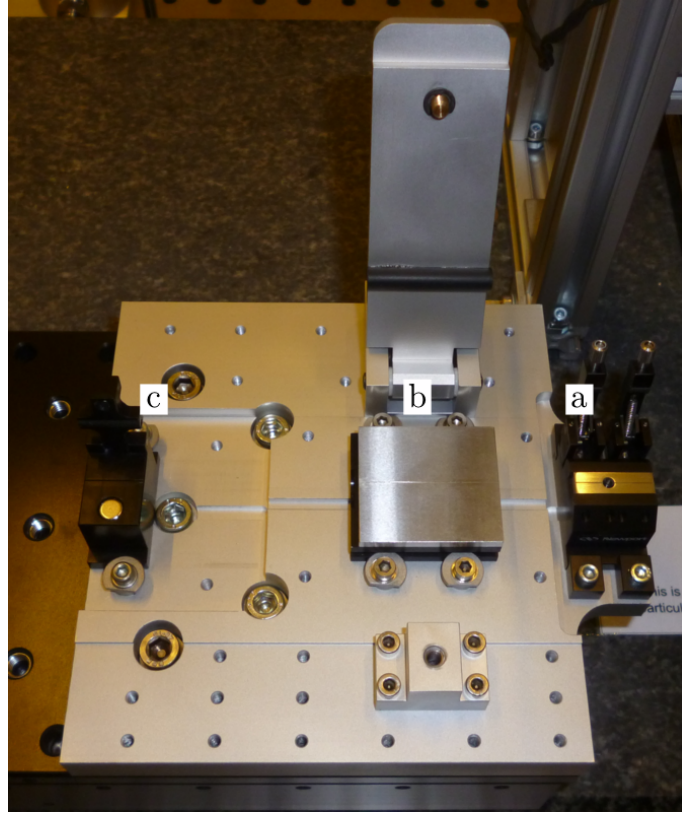


Figure 3.4. Fiber fixation platform together with the three dedicated fiber clamps for fine alignment (a), strong clamping (b) and coarse alignment (c).

platforms. The angular positioning error is one order of magnitude below the typical taper angle for OMFs and can be neglected.

For comparison in Fig. 3.5 there is the fiber clamping mechanisms of the previously used setup. The clamping force is provided by strong magnets which fix the optical fiber in a metallic groove. These magnets are strong because their fixation force must prevent the fiber from slipping when the translation stages apply the pulling force. This leads to a challenging positioning procedure, which may cause irregularities during the fabrication process.

The field of fiber positioning suggests itself for closer investigation, too. The crucial distinctions between the current and the previous implementation are illustrated in Fig. 3.6. The main difference between the two presented configurations is the inertia of the moving components. It has an effect at the turning points of the flame brushing motion. In the case of the old setup one translation stage is mounted on top of the other so that in contrast to the current design a significantly higher load has to be accelerated and decelerated with every move. Moreover, the total height of that assembly is fairly large compared to the new design. This is an inescapable drawback of that configuration. In particular, in combination with the fiber pulling force acting off-center, which can be deduced from Fig. 3.7, pitch, roll, and yaw inaccuracies during the fabrication procedure of the OMFs are more likely to occur

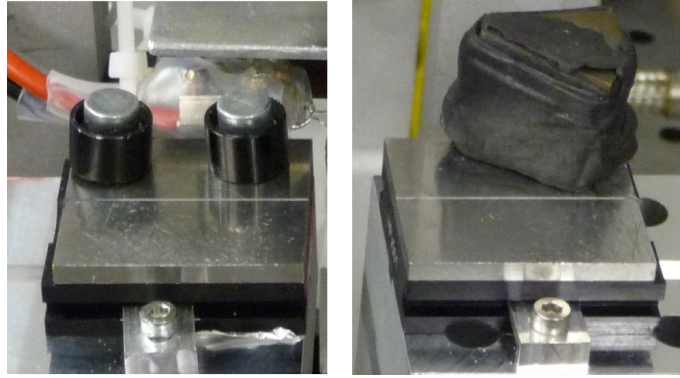


Figure 3.5. Fiber fixation mechanisms of the previously used fiber fabrication setup, strong magnets provide the clamping force.

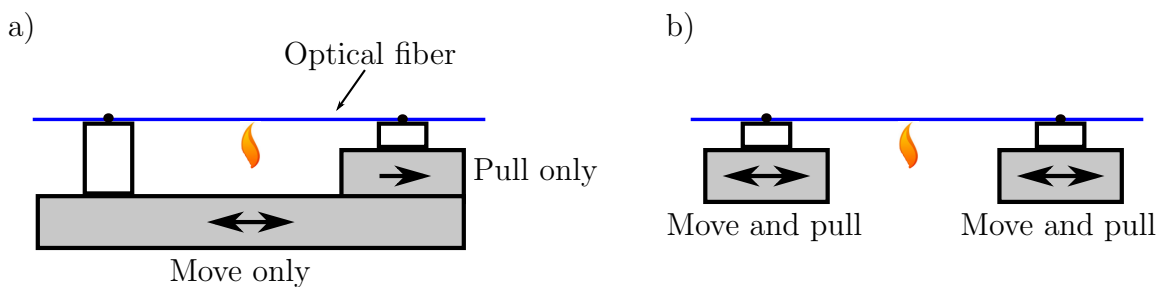


Figure 3.6. Two possible setups which allow to flame brush the optical fiber with a stationary flame. The previous configuration (a) uses one of the translation stages to elongate the fiber and the second stage moves the entire fiber fixation bidirectionally [13]. The current configuration (b) puts each end of the optical fiber on an own translation stage.

compared to the current design. These possible inaccuracies can be a reason for the recently observed limits of reliability [11] of the setup, which was used until now.

Comparing the two possible configurations from Fig. 3.6, one could argue that potential intrinsic positioning inaccuracies of the translation stages can have a larger effect in the new assembly. This could be because both translation stages perform the bidirectional motion. Only one translation stage moves bidirectionally in the previous configuration. Consequently, the elongation of the fiber can be controlled more precisely possibly. But this potential drawback of the new design can be overcome easily with the translation stages being chosen according to exactly these needs.

3.3. Gas burner and fuel supply system

A gas burner is often used as a heat source to process optical fibers [13, 16, 20]. The gas burner for this setup uses premixed ultra clean hydrogen and oxygen to avoid pollution of the OMF. Surface contaminations could lower the light transmission of the OMF. The thin waist can be destroyed when too much light is absorbed

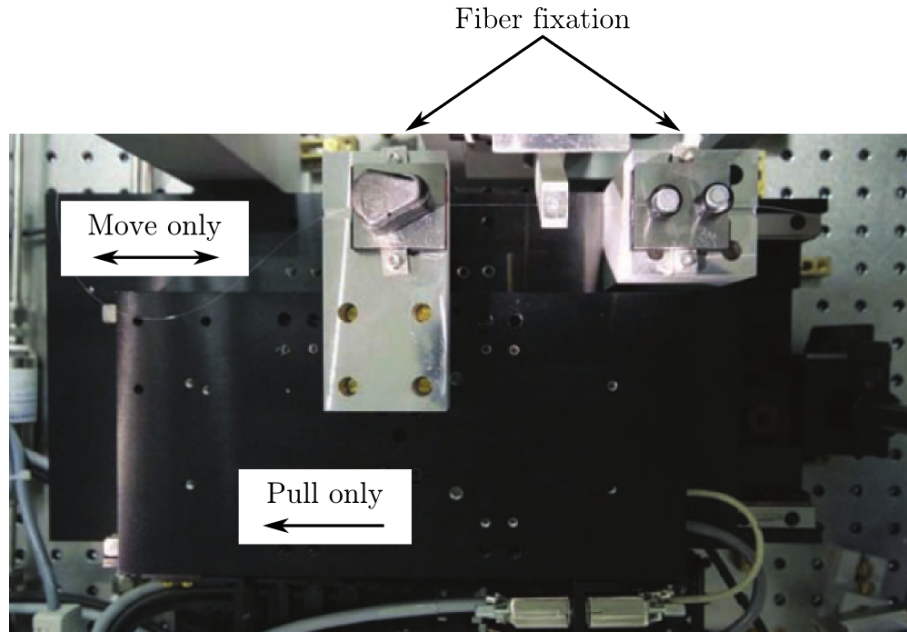


Figure 3.7. Top view on the previous OMF fabrication assembly, taken from [26].

and its energy is deposited in the fiber material. The maximum temperature of an oxygen-hydrogen flame is as high as 3050 °C [27]. This is sufficient for processing fused silica (cf. section 2.4).

The gas burner (see Fig. 3.8) is made from copper and mounted to a third motorized translation stage. The translation stage is needed to move the gas burner from the ignition position to the position of the optical fiber and back. Additionally, there is an ignition wire for reliable and clean electric flame ignition. The wire is made from a platinum-tungsten alloy (Pt92/W8). Platinum can withstand the self-ignition temperature of the hydrogen-oxygen mixture of 560 °C [28]. I chose this particular alloy with tungsten because its specific electric resistance is 30% higher compared to pure platinum [29]. As a consequence, a lower electrical current ($I \approx 6$ A) is needed to obtain the same temperature for gas ignition.

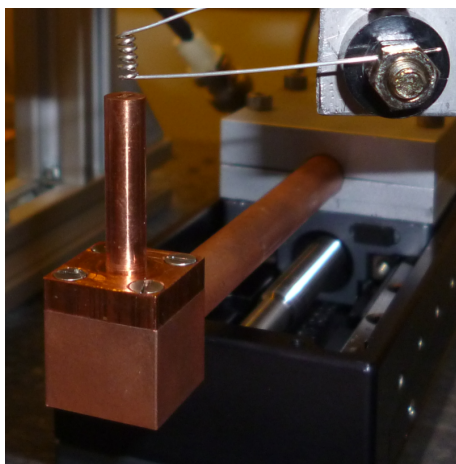


Figure 3.8. Gas burner with exchangeable nozzle mounted to a motorized translation stage to move the burner from the ignition position to the optical fiber. Just above the nozzle there is the ignition wire.

In contrast to intuition one must not use a single gas outlet hole of large diameter for the combustion of hydrogen with oxygen. Instead, one has to use multiple holes of small diameter. This is to prevent flashbacks of the combustion into the fuel supply tubing. For this, the so-called quenching distance is to be considered. It reflects the fact that in the direct vicinity to solid matter no combustion can take place. This is because close to solid matter the heat is conducted away from the flame at a high rate and ions of the combustion are captured. For hydrogen the quenching distance is found to be around 0.5 mm [27] to 0.7 mm [28]. Therefore, the gas outlet holes of the nozzle must be of correspondingly small in diameter – to be on the same side the diameter must not exceed 1 mm. For comparison with methane, as often used for fuel in home applications, the corresponding quenching distance is larger and allows safe use of gas outlet holes with diameters up to 4 mm [28].

I designed the gas burner such that the nozzle is exchangeable. This allows testing different layouts of gas outlet holes in the nozzle. With the nozzle of the gas burner in the previously used fabrication setup it is observed that the soft OMF shakes in the flame by tens of micrometers and moves upward [30]. This happens typically only in the last steps of fabrication, when the fiber diameter is already in the single micrometer regime. This can be caused by possible turbulences resulting from the particular design of the nozzle or the pressure of the gas flow. However, the shaking introduces uncontrolled elongation of the optical fiber, and the fused silica viscosity can vary when the fiber moves through the temperature gradient in the flame volume. This may limit the repeatability of the fabrication process.

As a possible solution I designed two alternative nozzles. These nozzles use gas outlet holes of different diameters to increase the gas flow locally. The differences in the layouts of the gas outlet holes are developed with the 3D CAD software **SolidWorks 2011 Student Edition**, which can simulate air flow. However, this software neglects combustion. The results of the air flow simulation and the underlying gas outlet holes can be seen in Fig. 3.9. The nozzle with outlet holes of equal diameter of $150\ \mu\text{m}$ (see Fig. (3.9b, (i))) is a remake of the burner used in the previous OMF fabrication setup [13]. The corresponding flow simulation shows that the gas escapes at approximately uniform velocity from the outlet area.

The size of the gas outlet holes for nozzles (ii) and (iii) varies between diameters of $150\ \mu\text{m}$ and $300\ \mu\text{m}$, in accordance with the quenching distance. As shown in Fig. 3.9a nozzle (ii) appears to create a V-shaped gas flow. This can stabilize the optical fiber in the central position to minimize position fluctuations. In contrast to that, nozzle (iii) spatially confines most of the gas flow to the central region of the nozzle. This flow can be exploited to stabilize the optical fiber with the help of the Coandă effect [31]. This effect describes the interaction of a jet with any solid matter surface placed in close vicinity. When nozzle (iii) is operated at a specific flow, which is fiber-diameter-dependent and to be determined experimentally, the higher gas flow velocity at the center of the nozzle can provide an attractive force for the fiber. This force acts in a layer perpendicular to the direction of gas flow. Because of this intrinsic centering of the fiber possibly a higher in-position stability of the OMF can be reached.

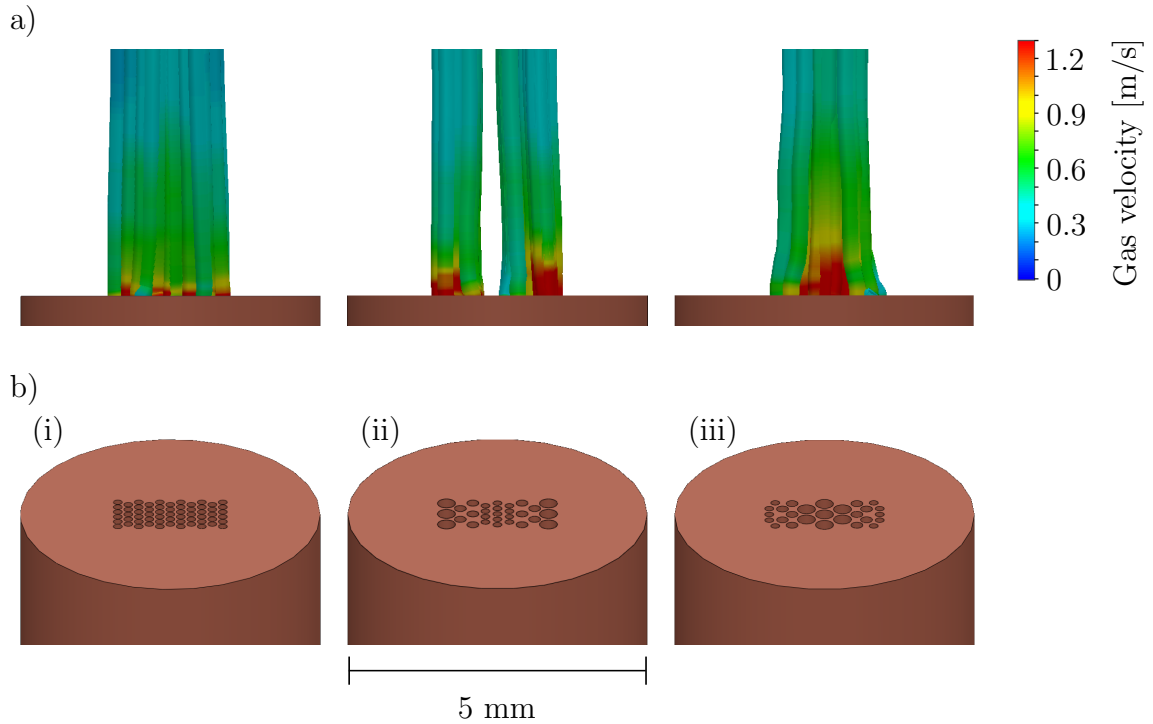


Figure 3.9. Different nozzles for the gas burner; a) simulated gas flow (total flow 100 ml/min, no combustion) for each nozzle, b) corresponding layout of the gas outlet holes.

In spite of the different sizes of the gas outlet holes, all nozzles have in common that the holes are confined to an area of 1 mm by 2 mm. The total area of holes is approximately 1 mm^2 for each nozzle. These common properties are to make sure that the heating effect on the fiber is approximately equal for all nozzles. The nozzles are supposed to be mounted such that the fiber crosses the area with holes in the shortest way and through the center point.

For a high repeatability of the gas flame, very accurate flow controllers for hydrogen and oxygen were chosen (model F-201CV-100-ABD-33-V from the company **Bronkhorst Maettig**). The controllers can regulate the gas flows with an accuracy of below round $\pm 1\%$ throughout the entire scale of flow from 4 ml/min to 100 ml/min for each gas type [32]. This scale proved to be suitable in previous experiments [13]. To actually achieve the rated accuracy of the gas flow control, very constant input gas pressure is required. For this, two subsequent stages of pressure regulation are connected to the gas cylinders to supply the flow controllers, see Fig. 3.10.

The chosen gas flow controllers require an analogue electric input signal which is proportional to the gas flow value to be set. The current gas flow value can be determined from an analog feedback signal. This allows on-the-fly manipulation and verification of the hydrogen or oxygen gas flow during the fabrication process of an OMF.

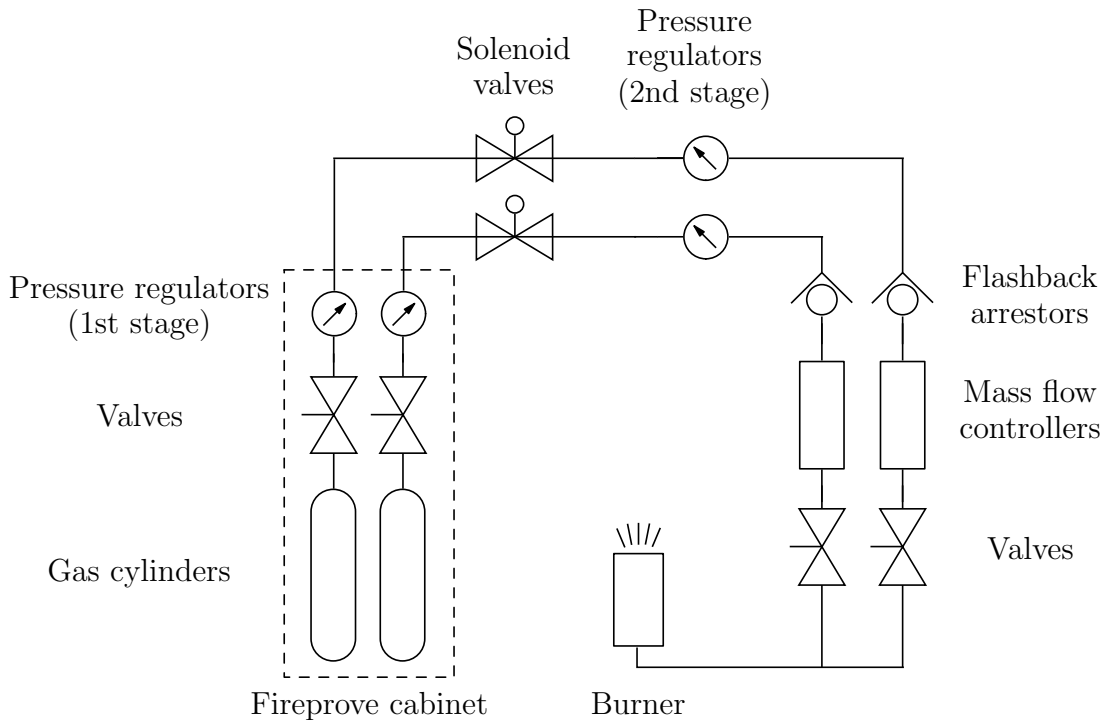


Figure 3.10. Gas supply system of the burner. The gas cylinders are stored in a fire prove cabinet, the solenoid valves are controlled by the gas warning system. All together round 30m of tubing is used.

For pressurized gas cylinders and the storage of flammable gases there exist detailed laws and safety regulations.⁹ According to these regulations the hydrogen and oxygen gas cylinders are stored in a dedicated cabinet. It is fire-prove for at least 90 min and connected to an exhaust air system to ensure that the air volume inside is exchanged at the required rate. Additionally, there is a gas warning system for the laboratory, which has got detectors for both hydrogen and oxygen.

3.4. Optical microscope

As shown already in the overview, this OMF fabrication assembly is equipped with an optical microscope. Its parts are drawn in Fig. 3.11. The microscope is build from an objective with long working distance (Mitutoyo, type Plan Apo, working distance 33.5 mm, resolution $1\ \mu\text{m}$ [33]), a focusing lens ($f = 150\text{ mm}$), and a black and white CCD camera (ImagingSource, model DMK 21BU04, from stock). The long working distance of the objective is required to keep enough distance to the gas burner when observing the fiber being flame brushed.

⁹For Germany these regulations are summarized in *TRG 280 (Technische Regeln Druckgase)*, “technical rules on pressurized gases”.

Besides, the entire microscope is mounted on a manual translation stage. This allows focusing the microscope on the surfaces of optical fibers with different diameters, or on the alignment groove below (see Fig. 3.12). Moreover, the microscope includes white light LEDs for illumination of the field of view.

The current combination of parts yields an optical magnification of 7.5 and an approximate magnification as large as 400 when using a standard computer screen to display the image. The field of view is $480\ \mu\text{m}$ by $360\ \mu\text{m}$.

To use this microscope for the analysis of the geometry of OMFs, the relation between the size of a feature in reality and in the microscope image has to be known. The conversion factor is determined with a silicon target¹⁰ to be $(0.748 \pm 0.006)\ \mu\text{m}/\text{px}$. Within its uncertainty the conversion factor equals the factor of $0.75\ \mu\text{m}/\text{px}$ which can be calculated from the properties of the components of the microscope.

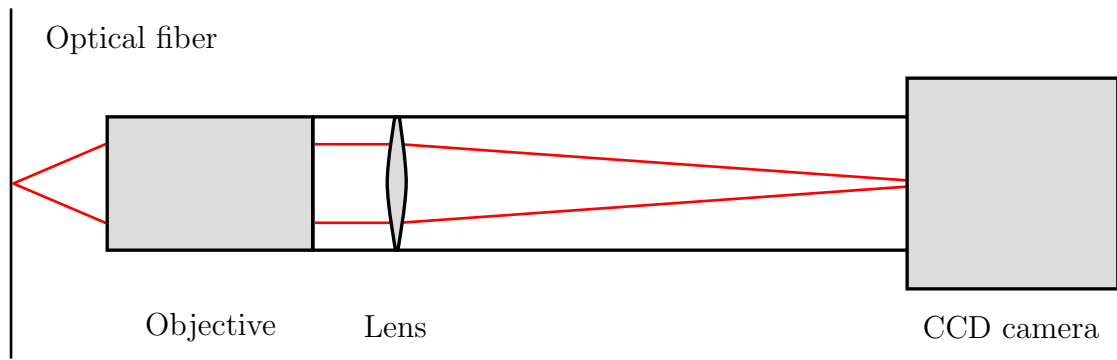


Figure 3.11. Microscope for imaging OMFs.

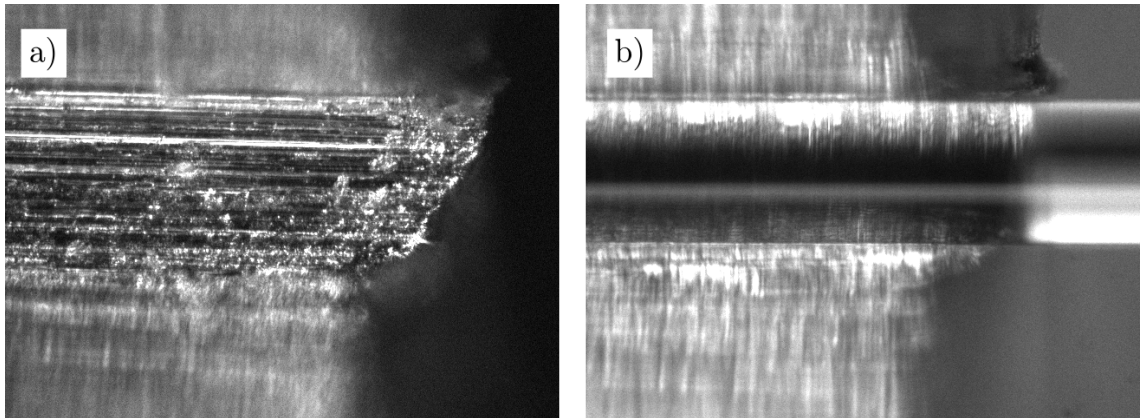


Figure 3.12. Innermost V-groove for fine alignment of the optical Fiber, a) focused to the metallic surface of the groove (no fiber), b) focused to an optical fiber ($D = 125\ \mu\text{m}$) inside the groove.

¹⁰More precisely, a comb-drive of a *MEMS* (*micro electromechanical system*) is used, which exhibits a periodic structure of appropriate dimensions.

3.5. Control electronics

I designed and fabricated a central controller (see Fig. 3.13) taking versatility and possible future extensions of the setup into account. It controls all parts¹¹ but the translation stages which have a proprietary controller and computer software.

The controller unit includes the power supplies which are needed for the different parts of the OMF fabrication assembly, and it uses an `mbed NXP LPC1768` microcontroller (cf. Fig. 3.14) to provide computer control for the outputs. It also can read out the status of the connected devices, such as the gas warning system. Most software controllable outputs are implemented as BNC connectors. They do not only allow the control of the currently used devices: nine out of 13 connectors in total are still available, some of them are already prepared as software controlled power outlets.

However, the two gas flow controllers require analogue signals for operation (cf. section 3.3). So addressing these devices with the `mbed` microcontroller is only possible via an additional digital to analogue converter. For this purpose, the model `AD5754` from `Analog Devices` is included on the circuit board. In spite of matching the specifications, it cannot be used with the `mbed` microcontroller. As a interim solution a standard laboratory power supply provides the set values for the gas flow controllers. Multimeters are used for the verification of the feedback values.

Together with the presented hardware, I developed a control software which is executed on the microcontroller. See appendix A.3 for the basics of the source code. This code is designed such that it evaluates user-given trigger commands to control the outputs of the `mbed`. These commands are exchanged between the computer and the microcontroller over a virtual serial connection via USB port. At the current stage of development a terminal emulator on the computer is used to send commands to the microcontroller or to display its feedback. The next goal is to establish a connection directly from `MATLAB` to the microcontroller. This would allow to merge the code for the microcontroller with the existing script for the flame brushing calculation, and to create a graphical user interface for the control software.

¹¹The control of auxiliary devices such as the flow box and the illumination is possible, too.



Figure 3.13. Central controller with power supplies and circuit boards. The front panel includes switches, connectors and indicators.

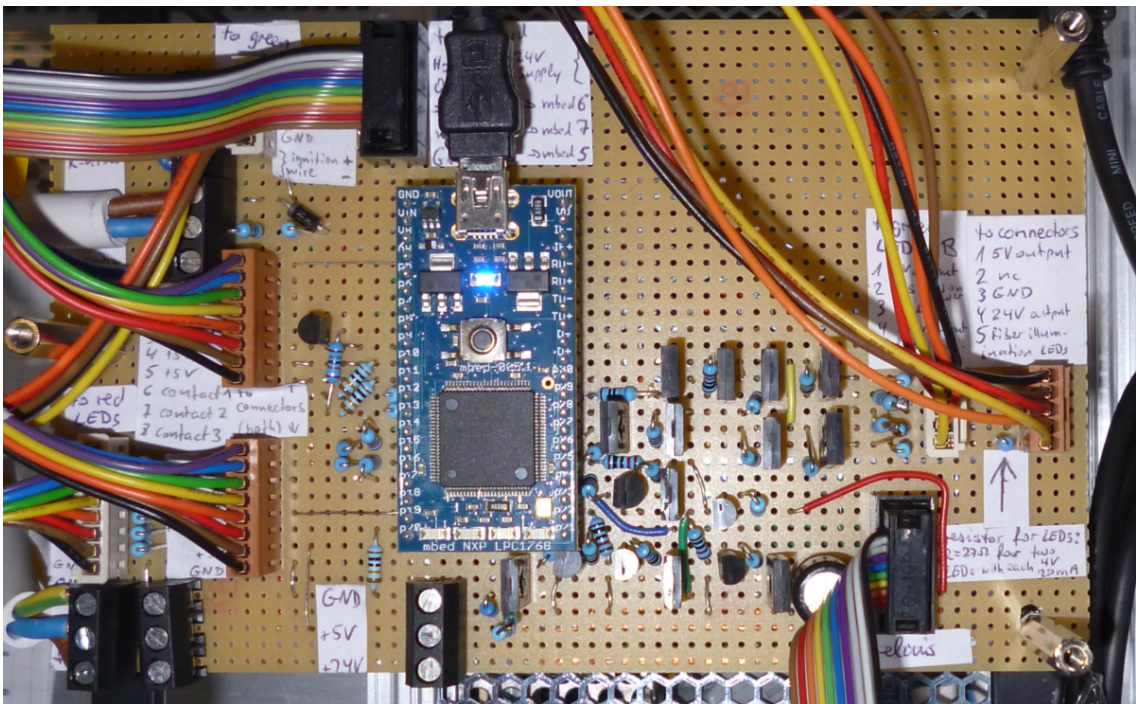


Figure 3.14. Main electronics board with the mbed microcontroller (blue chip at center position). The various cables connect to the power supplies, outputs, and indicators.

4. Effect of flame heating on the optical fiber

The optical fiber needs to be heated by the gas flame to a temperature, which allows deformation of the material but does not yet cause a loss of light transmission (compare section 2.4). To minimize the undesired effects of the gas flow on an OMF (cf. section 3.3), the stoichiometric ratio of hydrogen to oxygen gas flow of 2:1 is chosen. With this mixture ratio the smallest total gas flow is required for a fixed fiber temperature. Nevertheless, it can be advantageous to make the gas mixture slightly oxygen-rich. This is desirable for two reasons: First, the additional oxygen is available to burn any residual organic pollution on the of the optical fiber. These surface contaminations could be for example tiny residual coating particles. Second, silicon is commercially obtained when heating SiO_2 in a chemically reducing environment [21], which is avoided by a surplus of oxygen. The surplus of oxygen is chosen to be typically 1% of the total gas flow¹².

Two different experiments are performed to find a suitable gas flow for the fabrication of OMFs:

Heat fiber only In this procedure the optical fiber is exposed to the gas flame and one observes the light transmission, in particular when the fiber cools down. Potential effects of SiO_2 -crystallization, caused by a too high fiber temperature, would become visible as a decrease in transmittance in this test.

Heat and elongate fiber With this combination one directly sees at which gas flow the viscosity of the fused silica is low enough to allow deformation. A decrease in transmittance upon cooling-down can still be an indicator of a too hot fiber.

The transmittance of the optical fiber is measured with the setup, that is sketched in Fig. 4.1. It shows two extensions of the presented OMF fabrication assembly. One end of the optical fiber is connected to a white light source (a, **Avantes AVALIGHT-HAL**) the other end is connected to a spectrometer (b, **Avantes AvaSpec-2048x16**). Any decrease in transmittance can immediately be read off when using the transmittance of the optical fiber before beginning the experiment as a reference. It is observed that on the time scale of minutes the output power of the used light source may vary by up to 3%. Therefore, in the spectrum there can be an increase in transmittance above the reference level in addition to the noise.

¹²This approximation corresponds to the uncertainties of the gas flow controllers and their control unit (cf. sections 3.3 and 3.5). The oxygen of the surrounding air is not considered because it may not be available in the entire flame volume.

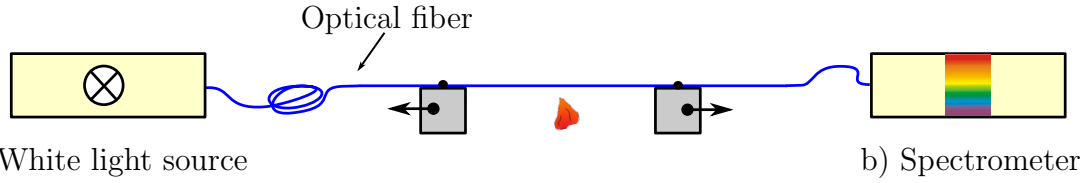


Figure 4.1. Measurement of the transmittance of the optical fiber while it is locally exposed to the gas flame.

For a first analysis in this thesis only nozzle (i) from Fig. 3.9 is employed, as it proved to be usable [13]. Figs. 4.2 and 4.3 show the transmission spectrum of the optical fiber when heating it. Flames with two different gas flow rates are applied for the time span of 5s each. Both plots show the transmittance spectrum before and after exposure of the optical fiber to the gas flame. No pulling force is applied.

In the case of Fig. 4.2 the gas flow mixture is $\text{H}_2 : \text{O}_2 = (86.0 \pm 0.1) \text{ ml/min} : (43.9 \pm 0.1) \text{ ml/min}$, so $(129.9 \pm 0.2) \text{ ml/min}$ all together. The total gas flow for the data presented in Fig. 4.3 is $(150 \pm 0.2) \text{ ml/min}$ with $\text{H}_2 : \text{O}_2 = (100.0 \pm 0.2) \text{ ml/min} : 50.0 \pm 0.1) \text{ ml/min}$.

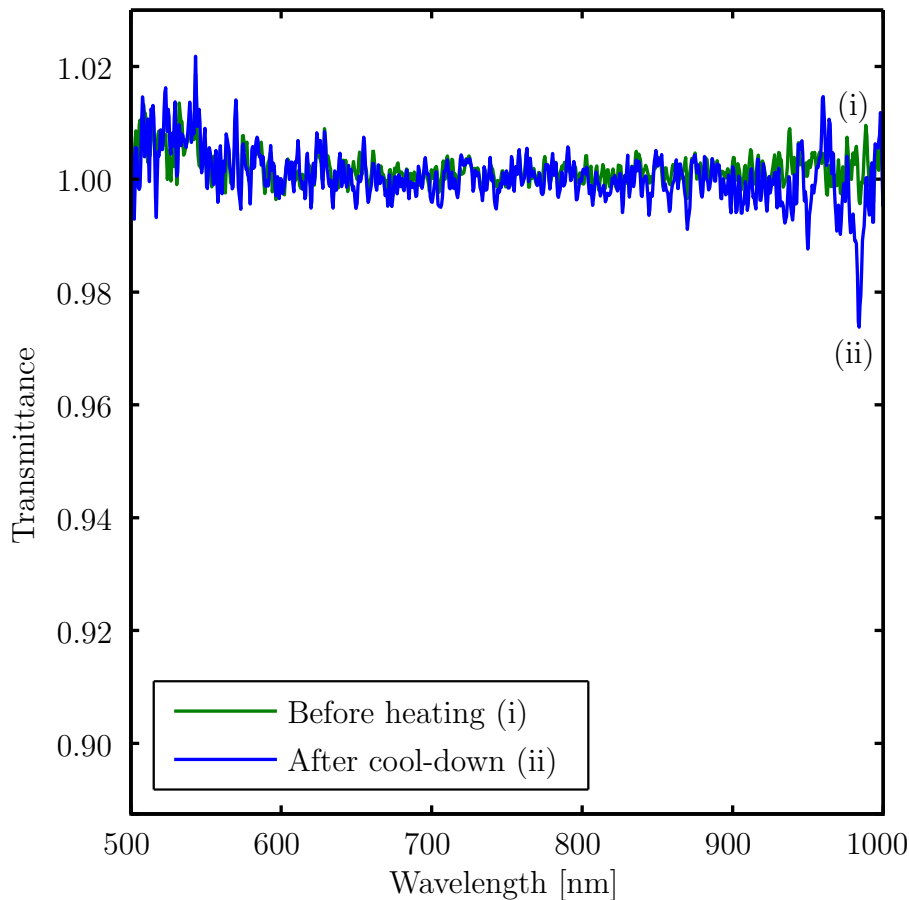


Figure 4.2. Transmittance spectrum of the optical fiber SM800 before and after exposure to a gas flame with a total gas flow rate of $(129.9 \pm 0.2) \text{ ml/min}$ and (almost) stoichiometric hydrogen-oxygen mixture.

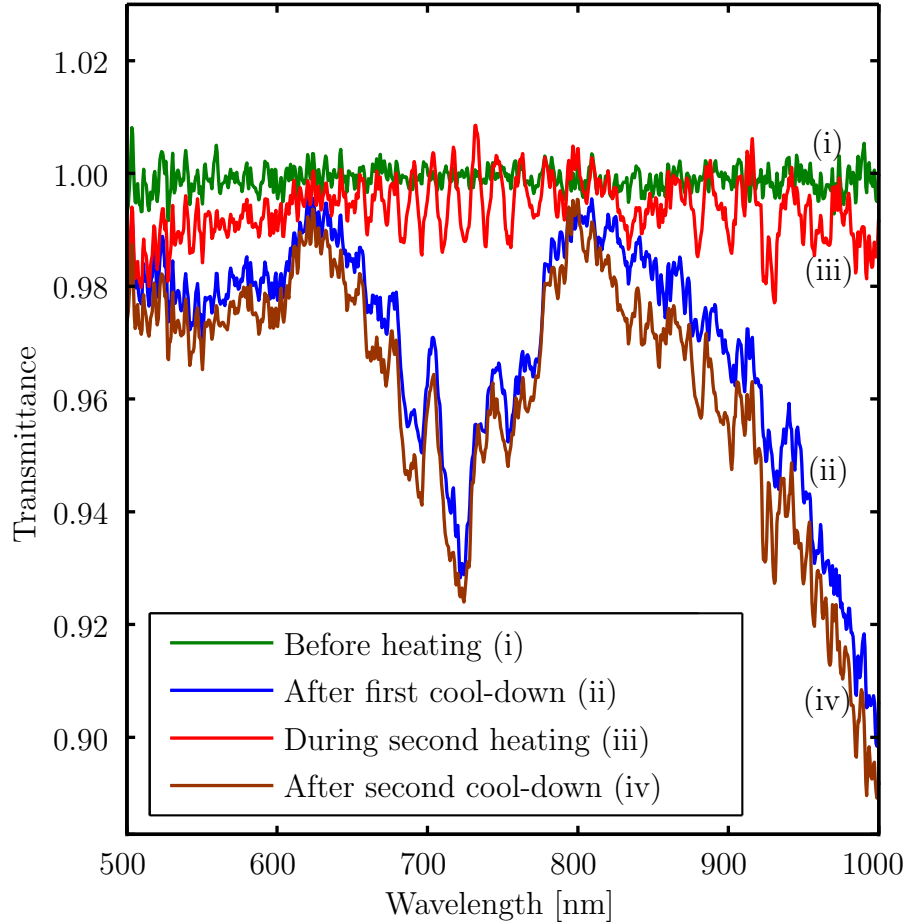


Figure 4.3. Transmittance spectrum of the optical fiber SM800 over two exposures to a gas flame with the total gas flow rate of (150.0 ± 0.2) ml/min, stoichiometric hydrogen-oxygen mixture.

Obviously, the heating effect of the flame with the smaller gas flow does not change the light guiding properties of the optical fiber significantly. Only for wavelengths around $\lambda = 960$ nm there is a fluctuation in transmittance which is larger than the usual noise level. This can result from the release of tensile stress from previous tests with the same piece of optical fiber.

In contrast to that measurement, with the higher gas flow a much stronger effect on the transmittance is observed. In Fig. 4.3 clearly a decrease in light transmittance can be seen after the cooling-down, in particular around $\lambda = 720$ nm and toward $\lambda = 1000$ nm. As the fiber is exposed to the same flame subsequently for a second time, one observes that the light transmittance is mostly restored. This strongly suggests that the observed decrease resulted from SiO_2 -crystallization (cf. section 2.4.1). The further decreased transmittance after the second down cooling may indicate that even more fused silica has been transferred to the crystal phase as a consequence of the second heating period. The interference fringes probably become visible because of thermal expansion of the optical fiber.

Heating and pulling the fiber symmetrically is combined to verify that tapering is possible at these gas flow rates. The total fiber elongation is chosen to be $800\ \mu\text{m}$. The processing time is approximately 8s, thus comparable to the previous tests. As before, almost stoichiometric gas mixtures are considered with a small oxygen excess. It is found that for all investigated gas flows the fiber temperature is sufficiently high to allow deformation. The resulting transmittance spectra of the optical fiber for various gas flow rates can be seen in Fig. 4.4. The uncertainty for all gas flows stated in the following is below $\pm 0.2\ \text{ml}/\text{min}$.

Comparing the spectra in Fig. 4.4 it is clear to see that the higher the total gas flow the smaller the light transmission of the optical fiber. As before, reheating the fiber can increase the transmittance. However, additionally the shape of the created tapers must be considered in this experiment with pulling. The tapers can be described by Eq. 2.3. Assuming a hot zone length of round $L = 0.8\ \text{mm}$ the resulting fiber diameter is approximately half of the initial diameter. This significant decrease in diameter over a short section along the fiber ($400\ \mu\text{m}$, half of the total elongation) introduces losses, too. Coupling to higher transverse or lossy modes can happen under these circumstances [17].

Moreover, the cut-off wavelength of the particular fiber must be considered. The fiber type is SM800 from **Fibercore**. It has a cut-off wavelength between $\lambda = 660\ \text{nm}$ and $\lambda = 800\ \text{nm}$ [34]. Therefore, toward the lower end of the investigated wavelength range interference between higher order modes is possible. Maybe this is the reason why in particular in Figs. 4.4a and 4.4b the transmittance after the processing is larger than before around $\lambda \approx 650\ \text{nm}$.

To distinguish which fraction of the transmission loss of the optical fiber results from heating and which fraction is due to tapering, some of the fibers are reheated to melt potential quartz crystals. The reheating indeed increases the light transmittance clearly, in particular in Figs. 4.4b and 4.4c. However, the average level of restored transmittance is below what was seen in the case of only heating the fiber (compare with Fig. 4.3). The deviation can result from losses at the fiber tapers or at the parts of the fiber which were pulled out of the flame and are not reheated.

However, Fig. 4.4d appears to be a special case. The transmittance hardly decreases after the second down-cooling. It approximately equals the transmittance during reheating the optical fiber in Figs. 4.4b and 4.4c. This suggests that here no crystallization has occurred but the observable decrease in light transmission rather results from the taper shape. The comparison to the previous experiment (heating only) reveals that no transmission loss was observed (cf. Fig. 4.2) at this gas flow rate.

Only stoichiometric mixtures of hydrogen and oxygen were chosen until now. One would expect that a higher total flow is required to obtain the same temperature of the optical fiber with equal gas flow rates instead. In agreement with this assumption, at a total gas flow rate as high as $180\ \text{ml}/\text{min}$ (mixture ratio 1 : 1) no significant change in the transmission spectrum of the fiber was observed.

To summarize, at all investigated gas flow rates inelastic deformation of the optical fiber was possible with the combination of the present nozzle and the available tapering setup. At the total gas flow of round 130ml/min and almost stoichiometric hydrogen-oxygen mixture no loss in light transmission through the fiber results from heating.

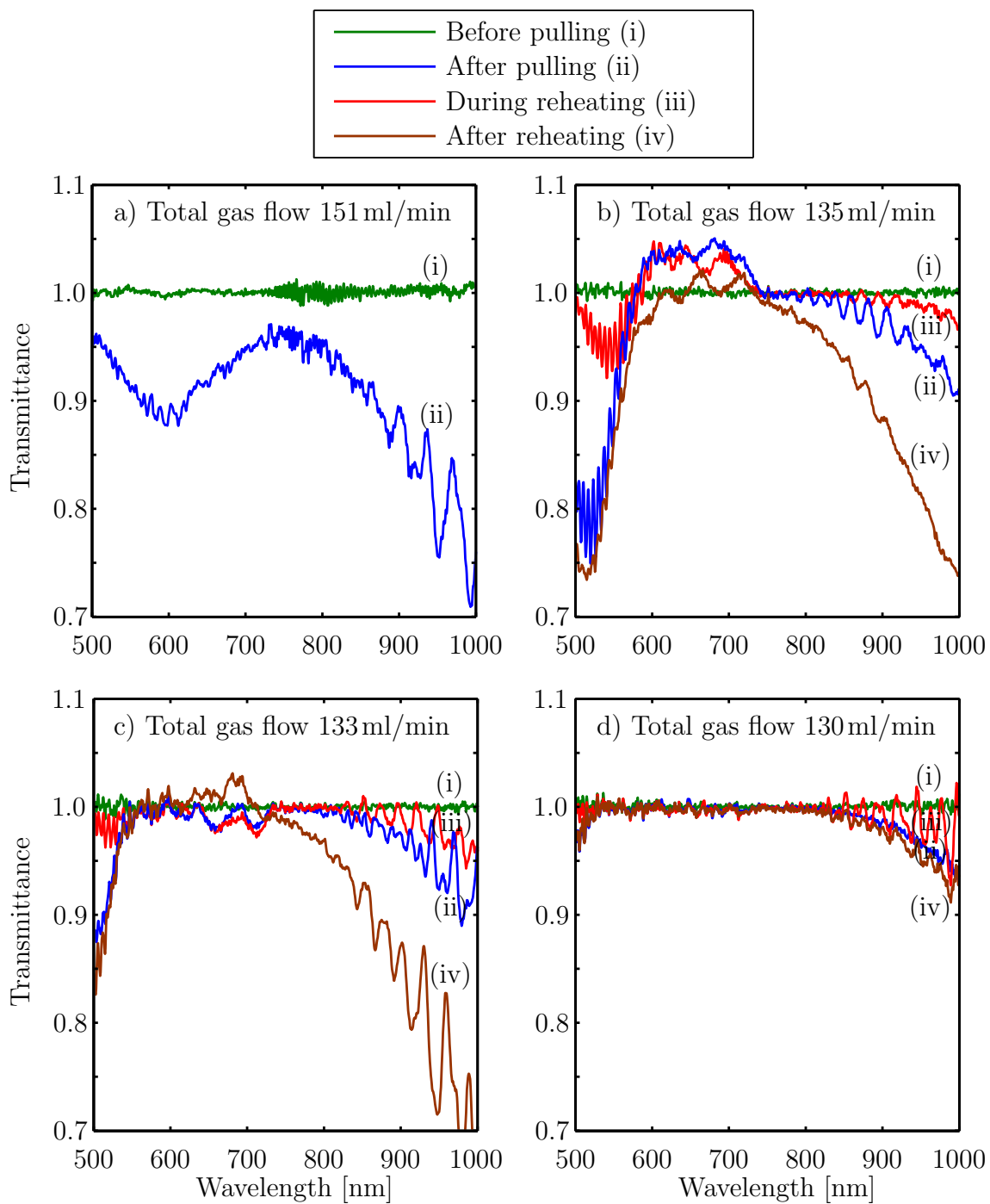


Figure 4.4. Transmittance spectra of the optical fiber SM800 after the exposition to flames with different total gas flow rates with (almost) stoichiometric hydrogen-oxygen mixture and an elongation of $800\ \mu\text{m}$.

5. Analysis of the microfibers

5.1. Light transmission

The transmission of light is the most important property of any OMF. It can be limited by various effects. The taper angle of the OMF must be shallow enough to allow adiabatic mode conversion [17]. A taper angle as low as a few milliradians is shallow enough to fulfill this criterion [13]. Moreover, possible crystallization of the fiber material (cf. chapter 4) or dirt on the fiber can introduce losses due to light scattering and absorption.

An exemplary analysis is prepared on an OMF with a waist diameter $D_w = 0.5 \mu\text{m}$ and a taper angle of $\Omega = 1.5 \text{ mrad}$. The fabrication parameters of this OMF are summarized in appendix B. The small taper angle makes sure that the light is fully adiabatic. For very small waist diameters $D_w < 0.25 \lambda$, additional guiding losses have been predicted [5, 35] and observed [14]. Thus, for the current waist diameter and the wavelength range considered here no such effect is expected.

The setup used to measure the OMF transmittance is the same as in the previous chapter (cf. Fig. 4.1). The bare optical fiber is thoroughly cleaned before starting the flame brushing to minimize the amount of potential dirt particles on the OMF. The obtained transmittance can be seen in Fig. 5.1. The wavelength region of interest is determined by the fiber material from which the OMF is made. For this SM800-fiber the cut-off wavelength is at $\lambda_{\text{cut-off}} = (660 \dots 800) \text{ nm}$, the operating wavelength is $\lambda = 800 \text{ nm}$ [34]. In the measured spectrum below $\lambda = 740 \text{ nm}$ the transmittance is significantly lower because of multi-mode interference of higher order transverse fiber modes. Above $\lambda \approx 1000 \text{ nm}$ the transmission of the SM800-fiber decreases strongly, so no usable transmittance signal can be obtained. On average in the infrared range between $\lambda = 750 \text{ nm}$ and $\lambda = 1000 \text{ nm}$ the transmittance is as high as 95.1%, with small fluctuations: $T_{\text{min}} = 93.6\%$ and $T_{\text{max}} = 96.3\%$. This transmittance of the OMF is suitable for all applications.

The slight decrease of the transmittance during the flame brushing process cannot be explained by a too high fiber temperature. The experiments in chapter 4 clearly predict a much stronger decrease when exceeding the optimum temperature multiple times.

More likely, the observed decrease is caused by unintended modulations in fiber diameter in spite of the shallow global taper slope. Such unintended very local changes in fiber diameter can exhibit large local taper angles. Therefore, non-adiabatic mode conversion may occur. To find possible deviations in shape along the OMF the tapers

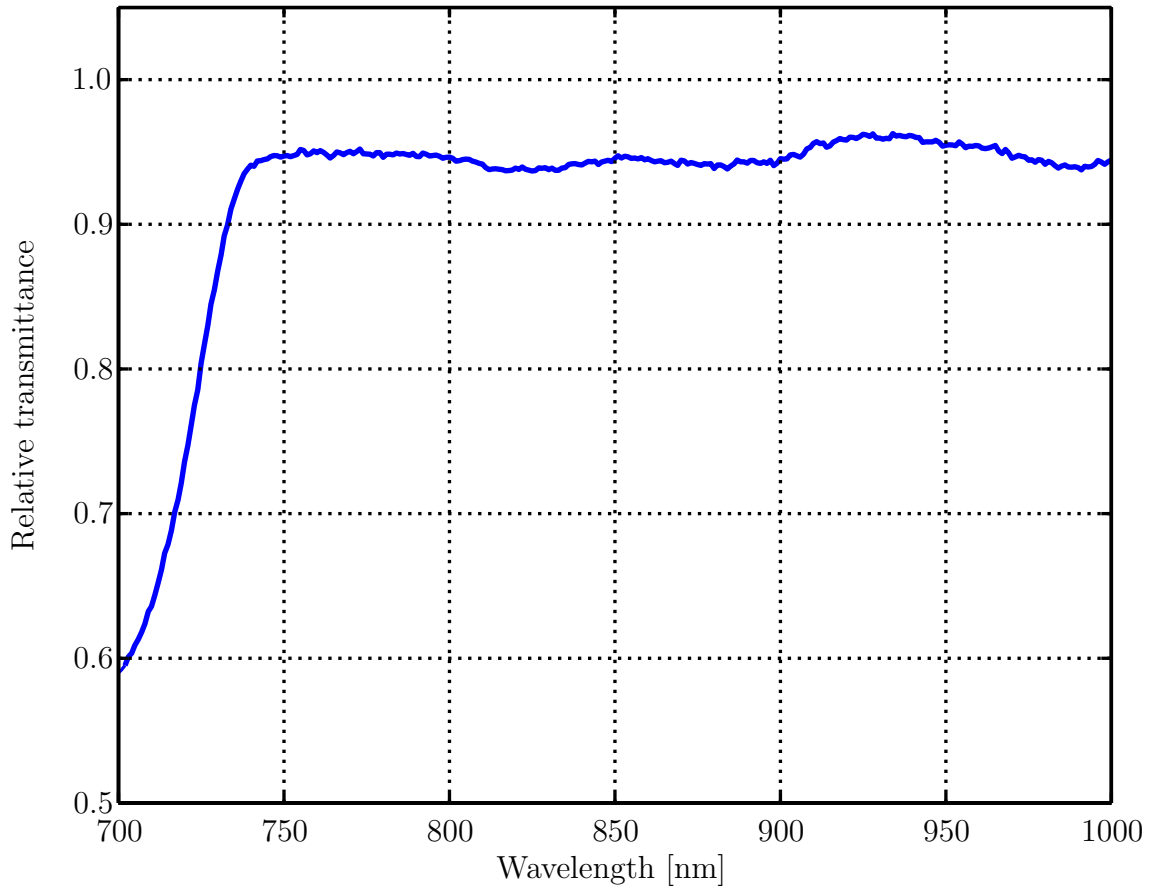


Figure 5.1. Transmittance spectrum of the OMF. The investigated wavelength range results from the properties of the fiber material (SM800).

are investigated closely. For this, the installed microscope can be used. When the motorized translation stages slowly move the entire OMF through the field of view, the fiber diameter along the tapers is found to change irregularly even though the OMF moves at constant velocity. The small steps can be seen only when the fiber moves. The height of these steps is at maximum on the order of a few micrometers. Very likely the observed structure on both taper sections is related to the brushing gap at the turning points of the flame motion during the fabrication procedure (cf. 2.3.2). The gap is not yet optimized and fixed merely indirectly.

5.2. General remarks on the shape analysis of the OMF

The OMF shape is what determines the light guidance properties. Therefore, exact knowledge of the fiber shape is desirable. There are different methods which allow to determine the diameter of an OMF: scanning electron microscopy [36], generation of higher harmonics [10], laser scattering at the OMF [37, 38], mechanical determination (see Fig. 5.2) or the use of an optical microscope as introduced in section 3.4. Within the scope of this thesis, the analysis of the fabricated OMFs is based on the optical microscope, which is implemented in the assembly. As a cross-check for some fibers a mechanical micrometer is used (Digimatic Micrometer Series 293 MDC-Lite from Mitutoyo).

The available optical microscope and the micrometer have almost equal accuracies. The measurement uncertainty of the micrometer is $\pm 2\mu\text{m}$, its resolution is $1\mu\text{m}$ [39]. Also for the digital image from the microscope the resolution is $1\mu\text{m}$ because of the long working distance objective [33]. When deducing the fiber diameter from a microscope image, the uncertainty is about $\pm(1.5 \dots 1.8)\mu\text{m}$. It follows via Gaussian error propagation from the position uncertainty of the edges of the OMF in the image and the uncertainty of the conversion factor ($\pm 2\text{px} \approx \pm 1.5\mu\text{m}$ and $\approx 0.8\%$ of the fiber diameter, respectively). Consequently, only OMFs, that are thicker than a few micrometer, are investigated. A typical microscope image of an OMF is shown in Fig. 5.3.



Figure 5.2. Measurement of the OMF waist diameter with the micrometer.

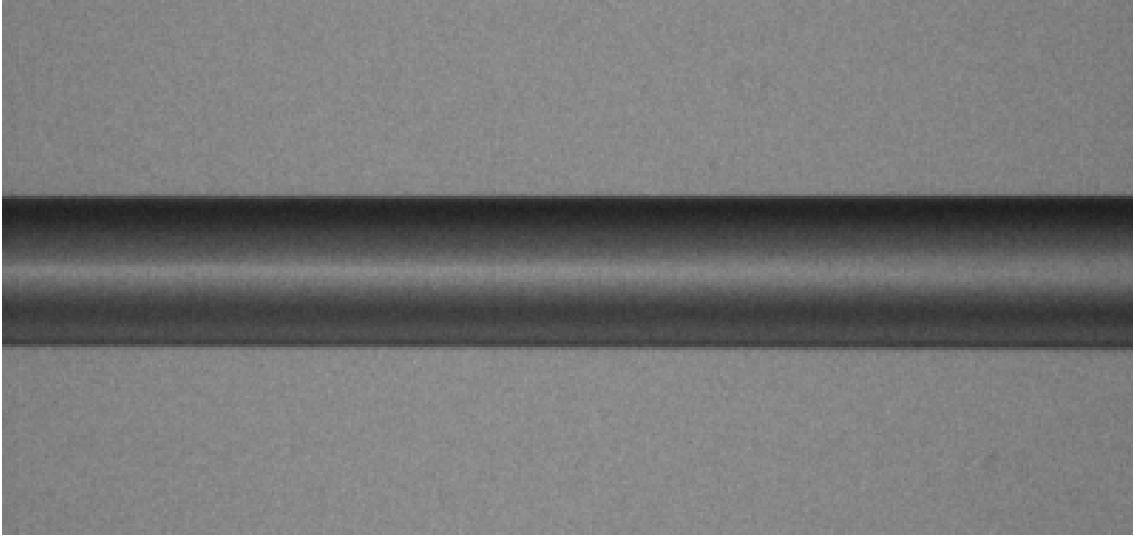


Figure 5.3. Microscope image of an OMF waist for diameter measurement. The evaluation yields $D_w = (62.8 \pm 1.6) \mu\text{m}$.

The OMFs for shape measurements are fabricated from the fiber type SMF-28 (manufacturer **Corning**). The initial diameter is $(125.0 \pm 0.7) \mu\text{m}$ [40]. However, for all OMFs the averaged initial diameter from microscope images is found to be $(126.3 \pm 1.8) \mu\text{m}$. No value below $125.6 \mu\text{m}$ occurs. In contrast to that with the same fiber material the micrometer yields an initial diameter of $(125 \pm 2) \mu\text{m}$. Both measured diameters match the specified diameter within the uncertainties. Nevertheless the difference between the two methods gives rise to the supposition that there is a systematic deviation of about $+1.3 \mu\text{m}$ in the case of the optical microscope. In the microscope image of the transparent fiber there appear shades and shines, which depend on the angle of illumination. Maybe diffraction of the illumination could be the reason. This could lead to the impression that in the microscope image any optical fiber appears larger than it actually is. None of the mentioned effects appeared with the silicon target used to calibrate the microscope (cf. section 3.4).

The result of a typical measurement of an OMF profile can be seen in Fig. 5.4. Every one or two millimeters along the OMF images are taken and evaluated to obtain the local fiber diameter. In this data set the first two millimeters along the fiber show the initial fiber diameter. Subsequently follow the down-taper, the waist and the up-taper.

It is to be said that for a smooth fiber surface the stripped fused silica fiber must be very clean and free of dirt particles. The microscope image in Fig. 5.5 shows a part of an OMF where the effect of pollution can be seen: After the flame brushing there is a small hump on the fiber. In the direct vicinity of the dirt particle the fiber diameter is smaller than elsewhere. The pollution is possibly a residual piece of the coating material which burned into the soft fused silica.

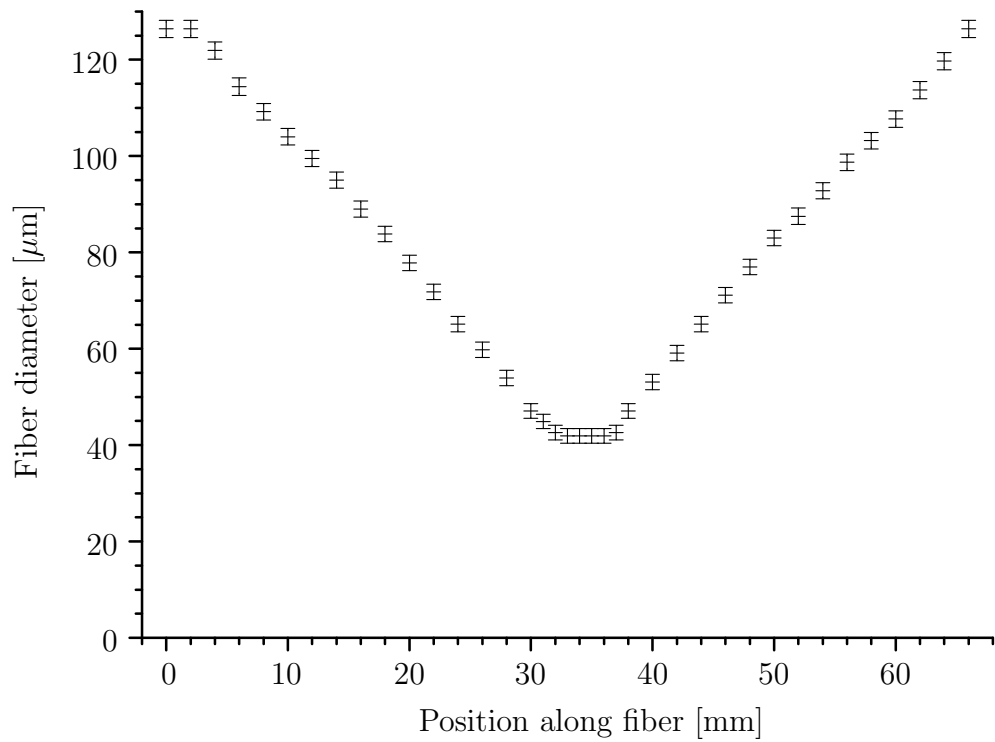


Figure 5.4. Profile of an OMF as obtained from microscope images along the fiber. The target diameter is $D_w = 40 \mu\text{m}$.

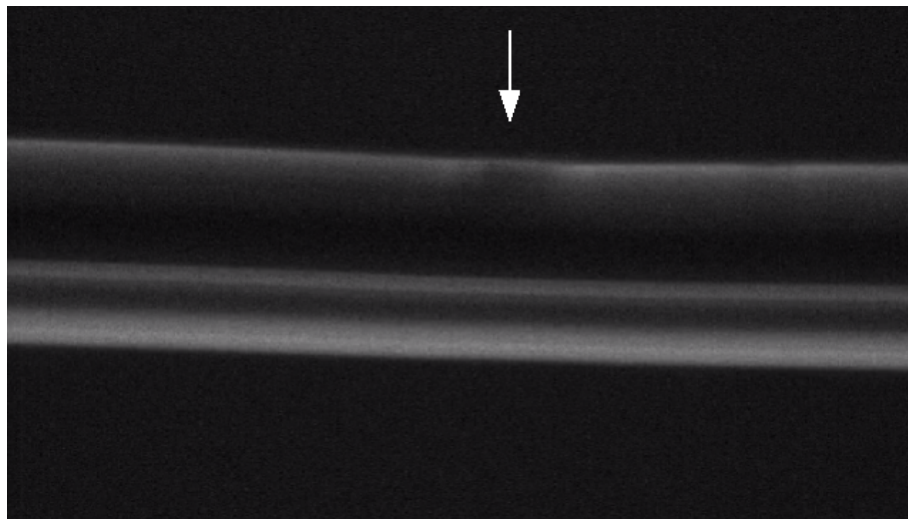


Figure 5.5. Section of an OMF with a local modulation in fiber diameter as a result of surface contamination.

5.3. Taper profile

Optical microfibers with linear taper sections and taper angles in the regime of a few milliradians are suitable for most applications. Therefore, in this section the evaluation is restricted to taper angles of $\Omega = 1.5$ mrad and $\Omega = 3.0$ mrad only.

The taper profile can be obtained from microscope images of the OMF. From plots of the acquired data, as in Fig. 5.4, the angles of down- and up-taper can be deduced. For that, linear functions are fitted to the corresponding data points. Six OMFs with constant linear tapers are evaluated in this manner. The obtained angles of down- and up-taper are symmetric (within the error bars) for each OMF, as expected. The averaged results for the two considered taper angles are summarized in Table 5.1. The comparison with the target angle shows that the obtained values are between 6% and 9% too small. A too shallow taper results from an exemplary verification with the mechanical micrometer, too.

Further investigation reveals that the measured data points do not strictly follow the linear fit function. There is a diameter-dependent systematic deviation observed for all OMFs. Above a threshold diameter at $D \approx (70 \dots 88) \mu\text{m}$ the local taper angle is smaller than the target angle. In contrast to that, below the threshold the taper slope is at minimum as steep as the desired value. The taper angle changes over a length of a few millimeters between the two sections of almost uniform slope.

In the following, two OMF samples are studied in more detail. Their exact properties can be found in appendix B. *Sample one* illustrates an extreme case of the deviation in taper angle (see Fig. 5.6). For the entire taper $\Omega_{\text{target}}^{\text{sample one}} = 3.0$ mrad holds true but the two independently fitted linear functions with the transition at $D = 80 \mu\text{m}$ yield

$$\Omega_{\text{measured}}^{\text{sample one}} = \begin{cases} (2.49 \pm 0.16) \text{ mrad} & D > 80 \mu\text{m} \\ (3.11 \pm 0.09) \text{ mrad} & D < 80 \mu\text{m}. \end{cases}$$

A similar result is obtained from *sample two*. It is designed to have two different slopes along each taper (see Fig. 5.7 for the measured profile). The intended transition is in the relevant range. The target angles for both taper sections are

$$\Omega_{\text{target}}^{\text{sample two}} = \begin{cases} 3.0 \text{ mrad} & D > 71 \mu\text{m} \\ 1.5 \text{ mrad} & D < 71 \mu\text{m} \end{cases}$$

Table 5.1. Averaged taper angles from multiple OMFs. The angles are obtained with linear fits to all the data points of the taper section.

Target angle [mrad]	Avg. measured angle [mrad]
1.5	down: 1.42 ± 0.03
	up: 1.41 ± 0.03
3.0	down: 2.80 ± 0.04
	up: 2.74 ± 0.05

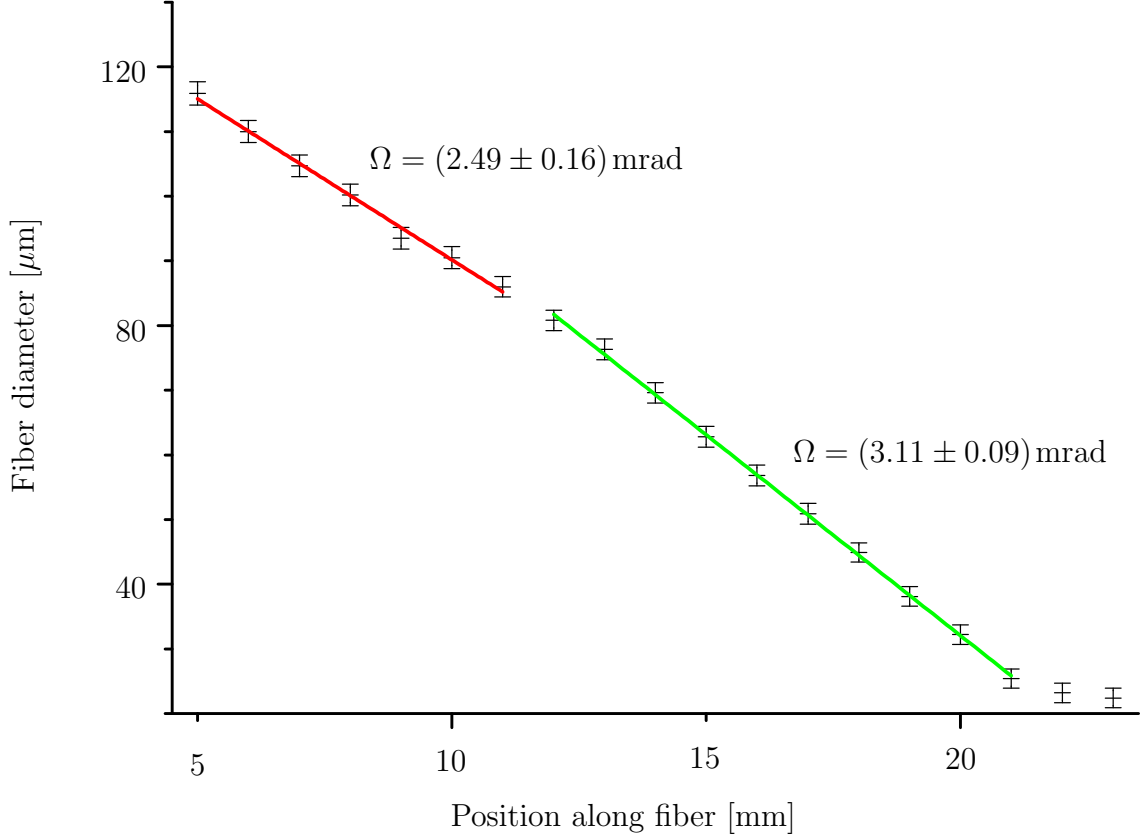


Figure 5.6. Close-up on the down-taper of *sample one*. This particular sample clearly shows that there are two taper angles instead of only one ($\Omega_{\text{target}}^{\text{sample one}} = 3.0 \text{ mrad}$) with the transition at $D \approx 80 \mu\text{m}$. The individual taper angles are obtained with linear fit functions to the corresponding data points.

until $D_w = 40 \mu\text{m}$ is reached. The fabricated tapers are symmetric within their errors, and again the upper part of the taper is significantly shallower than expected. The deviation is as large as with *sample one*. Concerning the lower part of the taper the measured angle is very close to the target value. The average over down- and up-taper is

$$\Omega_{\text{measured}}^{\text{sample two}} = \begin{cases} (2.5 \pm 0.1) \text{ mrad} & D > 74 \mu\text{m} \\ (1.52 \pm 0.09) \text{ mrad} & D < 74 \mu\text{m} . \end{cases}$$

The change in taper angle occurs around $D = 74 \mu\text{m}$ in contrast to the designed position ($D = 71 \mu\text{m}$). The transition point is challenging to extract from the measured data and may be influenced by the deviation in taper slope, too.

To summarize, for all OMFs there is a difference between the desired taper profile and the measured shape. There are two possible explanations, which are related to each other:

Thermal conductivity along the fiber axis According to [20], the thermal conductivity along the fiber scales quadratically with the fiber diameter. So it is capable of causing a diameter-dependent deviation in the fiber profile. The

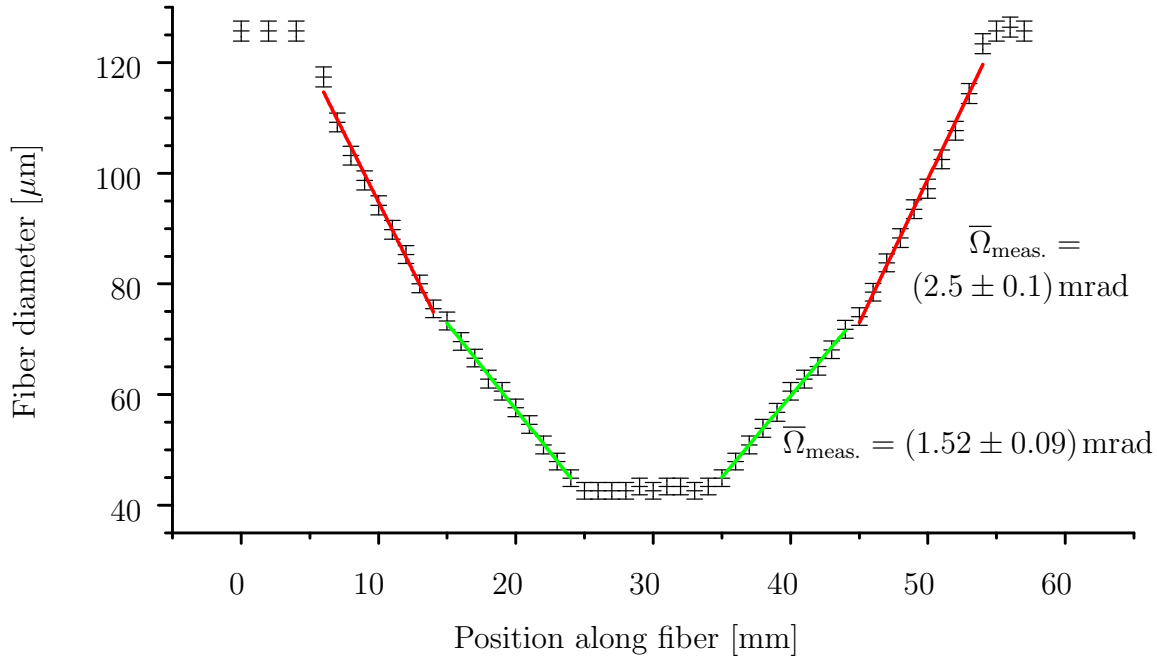


Figure 5.7. *Sample two* with a taper profile, that consists of two different angles. The desired angles are 3 mrad and 1.5 mrad for the upper and lower part, respectively. The measured angles are obtained with linear fit functions.

thermal conductivity along the optical fiber is largest at the initial fiber diameter and decreases as the fiber diameter decreases. This behavior approximately matches the observed deviation in shape.

Extension of the gas flame For the calculation of the flame brushing motion (cf. section 2.3.2) the center position of the flame is shifted until it reaches the maximum amplitude. Because of the possible extension of the real gas flame beyond this limit, too much fiber material may be heated. Therefore, the flame brushing amplitude, that the optical fiber experiences, could be systematically too large.

The influence of both assumptions can be tested with the calculations presented at the end of section 2.3.1. This algorithm can simulate the fiber taper profile which results from a given flame brushing amplitude. The brushing amplitude could be changed either by a constant amount or in a fiber-diameter-dependent manner. The constant change would correspond to the extension of the real gas flame, the dynamic modification could be used to simulate the effect of thermal conductivity along the fiber.

For detained analysis again *sample one* (Fig. 5.6) is investigated. The initial extension of the hot zone is round 14 mm. Its evolution during the fabrication process is manipulated in the two discussed ways. This can illustrate the effect of either one of the possible reasons for the observed deviation in taper profile. The simulation shows that only a combination of the two assumptions can cause the measured profile.

The best agreement with *sample one* is obtained with the following modifications of the original flame brushing amplitude:

- The brushing amplitude is continuously increased by 1 mm. This exactly corresponds to the extension of the gas outlet area along the optical fiber (cf. section 3.3).
- To include thermal conductivity along the fiber axis, the instantaneous hot zone length is increased by a dynamic value. The initial increase is 8% of the hot zone length. As a simple implementation, the increase becomes quadratically smaller as the fiber is elongated. Thus, it only scales approximately quadratically with the fiber diameter. However, the dynamic is chosen such that this increase reaches zero only at the (virtual) fiber elongation for $D = 0$, so when the thermal conductivity vanishes.

The resulting simulated taper profile is shown in Fig. 5.8. Two linear functions are fitted to the taper to obtain the corresponding taper angles. With the transition again at $D = 80 \mu\text{m}$ it follows

$$\Omega_{\text{simulated}} = \begin{cases} 2.5 \text{ mrad} & D \geq 80 \mu\text{m} \\ 3 \text{ mrad} & D < 80 \mu\text{m}. \end{cases}$$

As one can see, the taper simulation with thermal conductivity and extension of the flame yields the observed taper angle of *sample one* and *sample two* for the upper section of the taper. The slope of the linear function for the lower part of the taper does not fully equal to the taper angle of *sample one*. Maybe this is because the simulated effect of thermal conductivity does not strictly scale quadratically with the fiber diameter. Yet, it confirms the general finding that for smaller fiber diameters the taper becomes steeper.

Up to now, only the general slope along the taper of an OMF has been investigated. The fine structure can be of interest, too (compare section 5.1). Again for a qualitative evaluation of the fine structure, several OMFs are observed with the microscope while they are moved through the field of view by the translation stages at a constant velocity. Along some of the OMFs a weak periodic modulation of the diameter in addition to the general change along the taper can be observed. This corresponds to what was observed at the OMF for the transmission measurement. However, at the tapers of *sample two* a restriction of the current state of the calculations becomes visible. At *sample two* the steps along the taper are slightly larger. This is probably because the brushing trips are distributed equally over the entire taper. Their distribution cannot be optimized for both occurring taper angles at the same time (cf. 2.3.2).

In addition to the taper fine structure also the transition regime from the initial diameter to the taper and from the taper to the waist diameter would be worth being investigated. With the current limitations in measurement accuracy and resolution the transitions cannot be resolved. One would expect the transitions to be rounded because of the steady transition from deformable fiber with low viscosity to the remaining material with high viscosity at the edges of the gas flame.

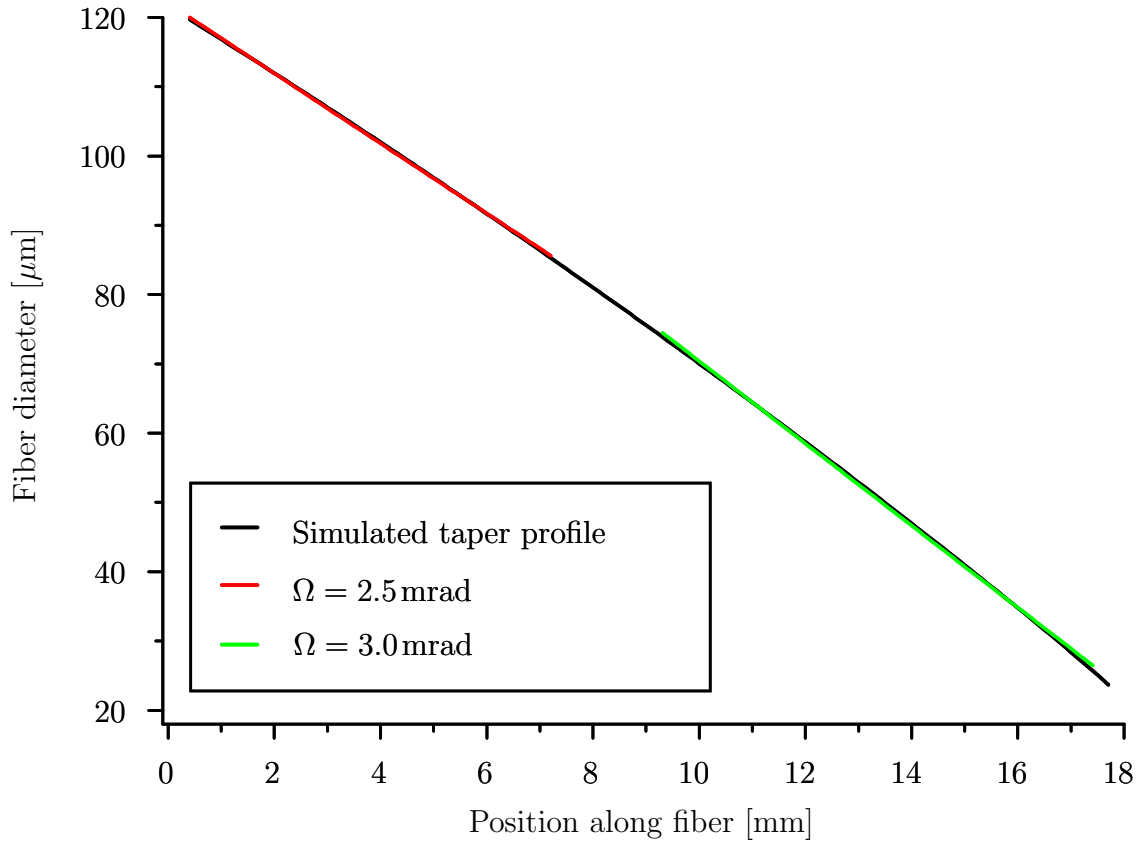


Figure 5.8. Simulated taper profile of *sample one* when an approximation of thermal conductivity along the fiber axis together with a flame extension of 1 mm is assumed.

5.4. Waist diameter

The waist diameter of an OMF determines the field distribution of the transmitted light (cf. Fig. 2.2). Therefore, several OMFs with target waist diameters between $D_w = 10\ \mu\text{m}$ and $D_w = 80\ \mu\text{m}$ are investigated to verify the fabrication accuracy. Thinner waist diameters can be fabricated, too (cf. section 5.1), but not analyzed with the used methods for data acquisition. For each waist diameter at minimum two samples are evaluated. For no investigated OMF the measured diameter along the waist is found to fluctuate by more than $1\ \mu\text{m}$. So the waist homogeneity is at minimum as good as the current measurement resolution and smaller than the measurement uncertainty.

A common procedure for all OMFs is used to obtain the average waist diameter from the microscope data. Only those data points contribute to the average waist diameter which lay within the error bar of the thinnest point along the fiber. This threshold makes sure that for every OMF the entire waist is taken into account but the transitions to the tapers are excluded, see Fig. 5.9 for illustration. However, for the cross-check measurements with the mechanical micrometer typically only one

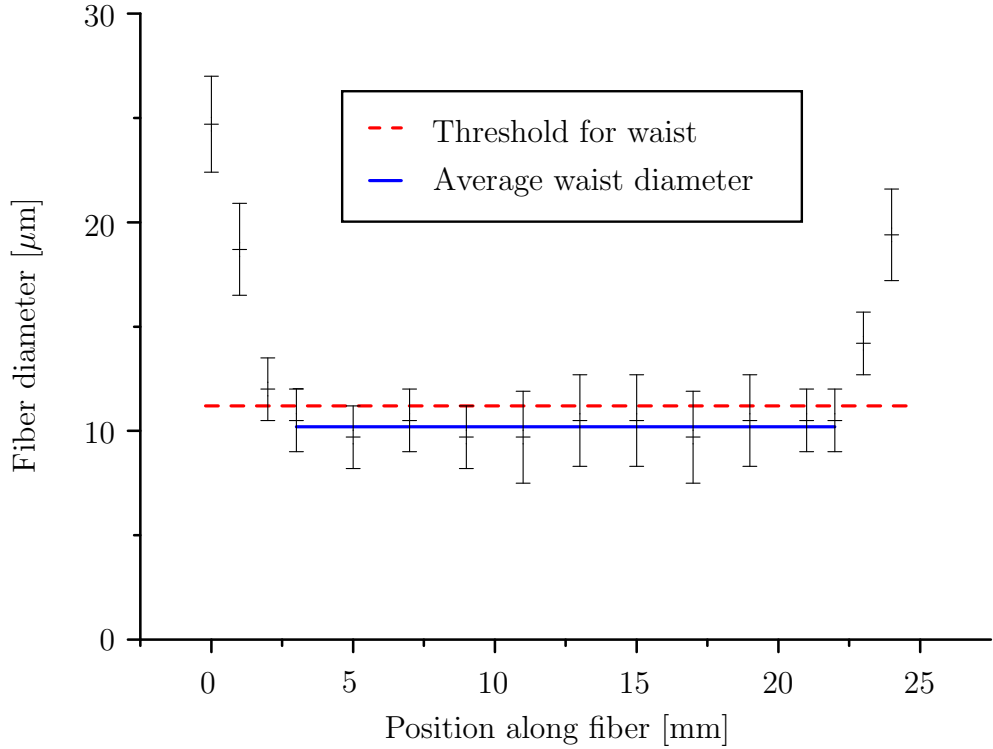


Figure 5.9. Close-up on the waist of *sample three*. The average waist diameter (solid blue line) is $D_w = (10.2 \pm 1.7) \mu\text{m}$. To the average diameter all data points below the threshold diameter (dashed red line) contribute. At this diameter the resolution of the microscope clearly limits the obtainable accuracy.

measurement point can be placed at the center of the waist. Moreover, this technique can only be used for OMFs with a waist longer than approximately 7 mm.

All waist diameters of the investigated OMFs are plotted in Fig. 5.10. The blue solid line indicates the target diameter. For all but one OMF the waist diameters are larger than the target values. The maximum deviation is $5.5 \mu\text{m}$ at $D_w = 80 \mu\text{m}$. The thinner the waist, the smaller the deviation. Only for the thinnest evaluated diameter the data points scatter around the target diameter. It is observed that for all fabricated waist diameters except for $D_w = 80 \mu\text{m}$ the measured values are confined to a range, that is smaller than the absolute value of the measurement uncertainty. This indicates that there are no significant deviations between different OMFs with same waist diameter. Moreover, there is no evidence found that the measurement with the microscope yields systematically larger fiber diameters than the mechanical micrometer, in contrast to the assumption in section 5.2. For detailed comparison, all the measured waist diameters sorted by target diameter and measurement method are put together in Table 5.2.

The deviation between the measured and the target values depends on the current fiber thickness. This is a similarity to the taper angle, which was investigated in the previous section. Indeed, the diameter-dependent deviation in waist diameter can be explained with the observed variation in taper angle along the OMF. The taper was found to be shallower than expected until approximately $D = 80 \mu\text{m}$. From there on

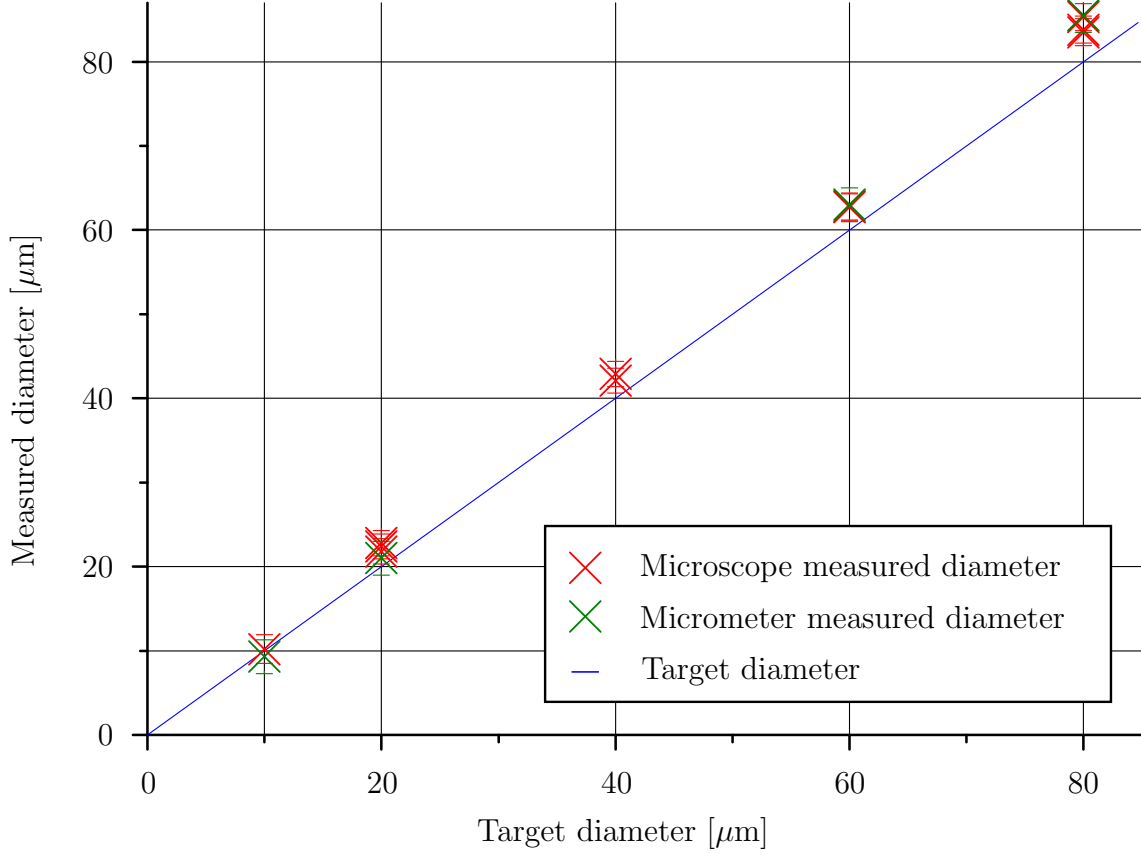


Figure 5.10. Comparison of the measured waist diameters of the OMFs with the target values.

it approaches the target angle and exceeds it at $D \lesssim 40 \mu\text{m}$ (see Fig. 5.8). However, the target taper angle is used to calculate the length of the taper, and thus the required fiber elongation. The fiber elongation is controlled precisely (cf. section 3.2). Consequently, the taper length can be assumed to match the desired length. Therefore, for any OMF with target diameter $D_w = 80 \mu\text{m}$ and its too shallow taper along the given taper length, the target waist diameter just cannot be reached.

This can be substantiated with an estimation. For a fixed taper length l_{taper} , the different waist diameters that result from two different taper angles are compared: Let the target taper angle be $\Omega_{\text{target}} = 3.0 \text{ mrad}$. Via the relation¹³

$$D(z) = D_0 - 2\Omega z$$

for $D_w = 80 \mu\text{m}$ follows $l_{\text{taper}} = 7.5 \text{ mm}$. In the worst case of *sample one*, the taper angle for $D = (125 \dots 80) \mu\text{m}$ is found to be $\Omega \approx 2.5 \text{ mrad}$. Consequently, with $l_{\text{taper}} = 7.5 \text{ mm}$ one expects here $D_w \approx 87.5 \mu\text{m}$. This estimation proves the assumed link between the deviations in taper angle and waist diameter. For the considered

¹³Note that for the small considered angles the taper slope equals the taper angle but the factor 2 is required because by definition the taper angle is measured from fiber edge to axis, thus related to the fiber radius.

Table 5.2. Measured OMF waist diameters sorted by target value and data acquisition method. When multiple OMFs with the same target waist diameter are investigated in identical manner, the given value is the average diameter.

Target waist diameter [μm]	Measured waist diameter [μm]	
80.0	microscope:	84.2 ± 1.6
	micrometer:	86 ± 2
60.0	microscope:	62.8 ± 1.6
	micrometer:	63 ± 2
40.0	microscope:	42.5 ± 1.5
20.0	microscope:	22.3 ± 1.5
	micrometer:	21 ± 2
10.0	microscope:	10.2 ± 1.7
	micrometer:	9 ± 2

extreme case the deviation in waist diameter is even larger than the maximum deviation in Fig. 5.10.

When thinner OMFs are fabricated, the taper angle increases toward the smaller fiber diameters. Therefore, the deviation in waist diameter decreases. Eventually, with the too steep taper for $D \lesssim 40 \mu\text{m}$ the observed initial increase in waist diameter exactly averages out at some waist diameter. This is approximately the case at $D_w = 10 \mu\text{m}$ where the measured waist diameter fits to the target value better than for any other diameter. Moreover, for even thinner OMFs one can expect the waist to be thinner than the target value because of the still increasing taper angle toward even smaller fiber diameters. However, this assumption cannot be proved in the context of this work.

5.5. Waist length

Another feature of the OMF geometry is the length of the waist section. Its exact value is not as important for the light guidance as the taper profile or the waist diameter. Nevertheless, the comparison of the waist length of an OMF with the desired value may help to discover and remedy possible inaccuracies during the fabrication procedure. For this, ten OMFs with the target waist length of $l_w = 5 \text{mm}$, $l_w = 10 \text{mm}$ or $l_w = 20 \text{mm}$ are evaluated. In principle, the waist length can be chosen freely. Here discrete steps are chosen to be able to compare the waist length of several OMFs with different waist diameters among each other.

It turns out that due to the used techniques no direct measurement of the waist length is possible. The exact position of the transition point from waist to taper cannot be resolved. However, one can suggest two evaluation methods, which allow the indirect determination of the waist length (see Fig. 5.11 for illustration):

1. The minimum length of the waist can be estimated from the data analysis for the waist diameter. There, all data points below a threshold were considered to be part of the OMF waist (cf. Fig. 5.9). The distance between the two outermost points that have a diameter below the threshold value can be assumed to be the minimum length of the waist. However, the waist may be almost as long as the entire distance between the first data points above the threshold, since the shape of the transition from the waist to the taper is unknown. Consequently, the uncertainty is approximately given by the distance between two adjacent data points when the waist length is estimated in this manner.
2. A different approach is to consider the intersection points of the obtained waist diameter with the linear functions fitted to the taper (points A and B in Fig. 5.11). The requirement of this estimation is precise knowledge of the taper profile, which was found to vary along the taper. Therefore, only the very thinnest section of the taper must be used to obtain the extrapolated local taper slope for the intersection region. Otherwise the obtained waist length can happen to be shorter than the minimum length from the first method. The uncertainty of the resulting waist length is determined by the uncertainties that are associated with the waist diameter and the linear functions, which approximate the taper.

For most OMFs the second method can be used, but for some samples only the combination of both methods yields reasonable values. This can be the case when very local changes in taper angle toward the waist occur. Then the linear fit functions do not indicate the transition points from waist to taper correctly. This is observed for instance with *sample four* (cf. Fig. 5.11). There is a deviation of 8% between the results of the two applied methods. The length of the waist appears to be at least 5 mm, which is the distance between the data points below the threshold diameter. However, the distance between the intersections of the average diameter and the extrapolated tapers is only (4.6 ± 0.3) mm. In such cases the minimum waist length, as obtained from the first method, is taken. There is no general tendency observed that the two presented evaluation methods return significantly different waist length for some waist diameter or a particular target length.

Therefore, for each of the three fabricated waist lengths the values from different OMFs are averaged. The results are summarized in Table 5.3. All the obtained waist lengths are found to match the target values within the uncertainty ranges. The uncertainties of up to approximately 10% result from the fact that only an indirect evaluation can be performed. A more precise determination of the waist length is needed to reveal potential deviations.

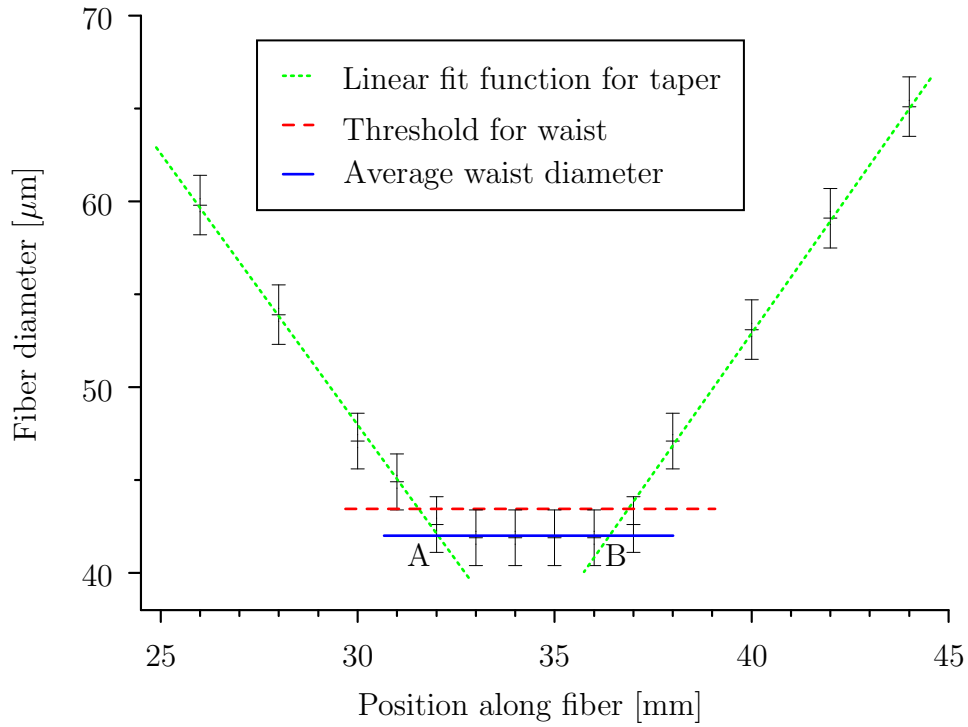


Figure 5.11. Close-up on the waist of *sample four*. The length of the waist strongly depends on the way it is extracted from the measured data. According to the first method, the waist length equals the distance between the data points below the threshold diameter (red dashed line). The second method uses the distance between the intersection points of the extrapolated tapers with the average waist diameter (points A and B). Here the two resulting waist length are found to differ by approximately 0.4 mm.

Table 5.3. Averaged waist length from multiple OMF.

Target waist length [mm]	Avg. measured waist length [mm]
5.0	4.6 ± 0.5
10.0	10.0 ± 1.1
20.0	19.8 ± 1.3

6. Summary and conclusion

A versatile fiber tapering setup was presented. It implements the *flame brushing technique*, in which the fiber is locally heated with a gas burner and elongated using two motorized translation stages. Together with the developed computer algorithm this allows the fabrication of OMFs with various geometries.

An optical microscope and a mechanical micrometer are used to verify the diameter profile of the OMFs fabricated. A systematic deviation between these two methods is suspected and requires further investigation. With the two methods, the coarse profile of the OMF can be determined. However, the obtainable accuracy and resolution does not allow detailed analysis of the entire OMF geometry. In particular, no OMF thinner than approximately $10\mu\text{m}$ can be analyzed. Nevertheless, it is found that for all OMFs the local taper angle deviates from the target value depending on the local fiber diameter. As a direct consequence, the obtained waist diameter does not match the expectation either. The origin of the observed deviation was verified successfully. The deviations in OMF shape arise because two aspects are neglected at the current state in the calculation of the flame brushing motion: The real extension of the gas flame and the thermal conductivity along the axis of the optical fiber.

Nevertheless, one must admit that – within the currently obtainable accuracy of verification – the shape parameters of the resulting OMFs scatter only a little. In addition to that, in the relevant wavelength range from 800nm to 1000nm the transmittance of an OMF was measured to be round 95%. So already at the current status the OMFs fabricated can be used.

7. Outlook

From the analysis of the optical microfibers, that have been fabricated up to now, one can derive a set of near-future improvements. The suggested aspects mainly focus on the algorithm, which calculates the motion commands, and the verification of the fabricated OMFs. These suggestions are first discussed together with general ideas for the optimization of the fabrication control. Then, future experiments are sketched.

7.1. Suggested improvements and extensions

As the analysis of the OMFs revealed, the algorithm, which calculates the flame brushing motion, has to be extended. It needs to take into account the real extension of the used flame and the thermal conductivity of the fiber material. These two aspects can be implemented by reducing the flame brushing amplitude by an effective flame extension. This effective flame extension is fiber-diameter-dependent. It can be obtained experimentally or from a simulation of the thermal conductivity along the fiber axis as in [20].

In addition to that, the distribution of the flame brushing trips along the fiber taper should be improved. The equal distribution along the fiber taper limits the fabrication accuracy of OMFs with varying angle along the taper. A more sophisticated approach has to be developed which takes into account the fiber taper profile.

At the current state several computer programs are required to control the hardware of the OMF fabrication assembly and to perform the required calculations. The goal is to be able to control the entire fabrication process with only one piece of software.

Concerning the verification of the diameter profile of the fabricated OMF there is a clear need for improvement. The scattering of a laser beam at the OMF allows to determine the fiber diameter with an accuracy below 50 nm [38]. The required setup can be implemented in the fabrication assembly. Another in-situ method to determine the fiber diameter during the fabrication procedure is the generation of higher harmonics as suggested in [15].

7.2. Possible future experiments

For more detailed studies of the effect of the gas flame on the optical fiber, the different nozzles available for the gas burner can be compared. A simulation of the gas flow which does include combustion can help to predict results and to find the optimum gas flow rates for these nozzles. For comparison a ceramic heater can also be used [41, 42].

By forming loops from the OMF waist, it is possible to obtain ring resonators [8]. One can align two or more of such resonators on a low refractive index substrate (e.g. magnesium fluoride). This provides coupled ring resonators, which could be used in cavity quantum electrodynamics experiments.

The presented fabrication assembly is very suitable to test OMFs as modal interferometers, because it allows including a bath with liquids. For example, one could combine the stretch- and in-liquid interferometry experiments described in [11]. The elastically stretching the OMF can be performed very precisely directly by the motorized translation stages just after the OMF has been fabricated.

In this thesis only OMFs with two tapers and the waist section in between are discussed. It is also possible to fabricate completely different kinds of modulation of the fiber diameter. For example, with a periodic structure of shallow fiber tapers, a long-period fiber Bragg grating can be created. Using a photonic crystal fiber, one can achieve slow light propagation with low loss in this way [43].

A. Source code

A.1. Source code of the flame brushing amplitude calculation

The following MATLAB script is used to calculate the entire flame brushing motion according to the desired diameter profile of the OMF. As the result it outputs a file which has to be copied to the control software Motion Composer of the Aerotech translation stages to have the sequence of motion executed.

User input

```
All length are given in micrometers.
zMin = 0; % for plots: smallest position on coordinate axis
zMax = 100000; % for plots: largest position on coordinate axis
zStep = 10; % elementary step on coordinate axis for computations
elongationGridStep = zStep; % elementary elongation
dMin = 0; % for plots
d0 = 125; % initial diameter
dWaist = 0.5; % waist diameter of OMF
lengthWaist = 5000; % length of waist of OMF

% Additional parameters only needed for the subsequent calculation of
% the brushing motion.
% Define how often the flame should travel along fiber:
numTrips = 86;
% Define how long the elongation of the fiber by one micrometer takes
% in units of seconds:
timePerMicronElongation = 0.018;

% Make given step size and initial values match:
zMax = zStep * ceil(zMax / zStep);
lengthWaist = zStep * ceil(lengthWaist / zStep);

% Profile of taper (same for down and up taper)
d = @(z) d0 - 0.003 * z; % example of linear slope

% Plot the fiber profile:
```

```

% Array along coordinate axis:
zArray = zMin: zStep: zMax;
% all diameters according to d(z) along the axis:
dArrayPlot = d(zArray);
% Coordinate zLimit at which waist diameter is reached:
z0 = interp1(dArrayPlot, zArray, dWaist);
% Coordinates for downtaper:
zArrayPlot1 = zMin: zStep: z0;
% Coordinates along waist:
zArrayPlot2 = ones(1, (lengthWaist / zStep) - 2) * z0;
% Coordinates for uptaper:
zArrayPlot3 = fliplr(zArrayPlot1);
% Coordinates for entire profile (with proper scale):
zArrayPlot = [zArrayPlot1, zArrayPlot2, zArrayPlot3] * zStep;
% Diameter along that profile:
dArrayPlot = d(zArrayPlot / zStep);

figure(1);
subplot(2, 2, 1);
plot(zStep * (zMin: 1: numel(zArrayPlot) - 1), dArrayPlot);
axis([zMin, (2 * z0 + lengthWaist), dMin, d0]);
title('Fiber profile');
ylabel('Fiber diameter [um]');
xlabel('Coordinate along OMF [um]');

```

Step 1

Calculate the size of the hot fiber zone as function of coordinate.

According to Eq. 26:

```

dSqr = @(z) d(z) .* d(z) .* 0.25;
lHotZoneCoordinate = @(z) dWaist .* dWaist .* 0.25 .* lengthWaist ...
    / (d(z) / 2) / (d(z) / 2) + 2 / (d(z) / 2) / (d(z) / 2) ...
    .* quadgk(dSqr,z,z0); % quadgk is numerical integration of a function
% Coordinate array with the length of the taper:
zArray = zMin: zStep: z0;
% Create array with hot zone size:
lHotZoneArrayCoordinate = zArray * NaN;
for s = zArray
    lHotZoneArrayCoordinate(s / zStep + 1) = lHotZoneCoordinate(s + 1);
end

% Plot result:
figure(1);

```

```

subplot(2,2,2);
plot(zArray, lHotZoneArrayCoordinate)
axis([zMin, z0, 0, max(lHotZoneArrayCoordinate)]);
title('Hot zone size as coordinate z along taper is created.');
```

ylabel('Hot zone size [um]');

xlabel('Coordinate along taper [um]');

```

% For further calculation determine initial value of hot zone size:
l0 = dWaist * dWaist * 0.25 * lengthWaist / (d0 / 2) / (d0 / 2) ...
    + 2 / (d0 / 2) / (d0 / 2) .* quadgk(dSqr, 0, z0);
```

Step 2

Calculate the current fiber elongation when the points along the taper are created.

According to Eq. 27:

```

x = @(z) 2 * z + lHotZoneCoordinate(z) - l0;
% Create Array with elongation as function of taper coordinate:
elongationArrayCoordinate = zArray * NaN;
for s = zArray
    elongationArrayCoordinate(s / zStep + 1) = x(s);
end

% Plot result:
figure(1);
subplot(2,2,3);
plot(zArray, elongationArrayCoordinate)
axis([zMin, z0, 0, max(elongationArrayCoordinate)]);
title('Current fiber elongation when point on taper is created');
```

ylabel('Fiber elongation [um]');

xlabel('Coordinate along taper [um]');

Step 3

Calculate the hot zone size (brushing amplitude) as function of fiber elongation.

According to Eq. 28:

```

lFlameElongation = @(x) x + l0 - 2 ...
    * interp1(elongationArrayCoordinate, zArray, x, 'spline');
```

% According to Eq. 29:

```

% elongationMax = 2 * z0 + lengthWaist - l0;
% Make elongationMax match elementary elongation:
elongationMax = elongationGridStep * numTrips ...
* ceil(max(elongationArrayCoordinate) / elongationGridStep / numTrips);
```

```

% Create Array with hot zone size as function of fiber elongation:
elongationGrid = 0: elongationGridStep: elongationMax;
lFlameArrayElongation = ones(size(elongationGrid)) * NaN;
for s = elongationGrid
    lFlameArrayElongation(s / elongationGridStep + 1) ...
    = lFlameElongation(s);
    % Display progress of calculation
    fprintf('\b\b\b\b\b\b\b\b\b\b\b\b');
    fprintf('%4.1f%% done.', 100 * s / max(elongationGrid));
end
% Plot result
figure(1);
subplot(2,2,4)
plot(elongationGrid,lFlameArrayElongation)
axis([0,x(z0),0,max(lFlameArrayElongation)]);
title('Hot zone size throughout the pulling process');
ylabel('Hot zone size [um]');
xlabel('Fiber elongation[um]');

```

A.2. Calculation of flame trips

The following source code bases on the previous code from appendix A.1. The variables and their values are still used in the following. Nevertheless, the specific parameters for the subsequent calculation are shown again for better understanding.

Additional parameters

```

% Define how often the flame should travel along fiber:
numTrips = 86;
% Define how long the elongation of the fiber by one micrometer takes
% in units of seconds:
timePerMicronElongation = 0.018;

```

Step 1

Symmetric lower and upper limits for the flame brushing are created from the flame brushing amplitude.

```

% Allocate memory
lowerFlameLimitArrayElongation ...
    = ones(1, elongationMax / elongationGridStep + 1) * NaN;
upperFlameLimitArrayElongation ...

```

```

    = ones(1, elongationMax / elongationGridStep + 1) * NaN;

% Give first entries
lowerFlameLimitArrayElongation(1) = 0;
upperFlameLimitArrayElongation(1) = lFlameArrayElongation(1);

% Calculate all other entries
s = 2; % starts at s = 2 because the first one is already filled
while (s < elongationMax / elongationGridStep + 2)
    lowerFlameLimitArrayElongation(s) ...
        = 0.5 * (lFlameArrayElongation(1) - lFlameArrayElongation(s));
    upperFlameLimitArrayElongation(s) ...
        = lowerFlameLimitArrayElongation(s) + lFlameArrayElongation(s);
    s = s + 1;
end;

```

Step 2

```

elongationPerTrip = elongationMax / numTrips;

```

Step 3

Move the flame position bidirectionally within the given limits.

```

% Allocate memory
flamePositionVsElongation = ones(1, elongationMax ...
    / elongationGridStep + 1) * NaN;

% Initial position at zero elongation at lower limit
flamePositionVsElongation(1) = 0;

% Calculate the first movement of the flame.
% flameMove is the movement per elementary fiber elongation step
flameMove = (upperFlameLimitArrayElongation( ...
    1 + elongationPerTrip / elongationGridStep) ...
    - lowerFlameLimitArrayElongation(1)) ...
    / (elongationPerTrip / elongationGridStep);

% Now the actual movement is calculated.
% The variable g tells if flameMove is to be recalculated at limit
g = 0;
currentElongationStep = 0;
while (currentElongationStep < elongationMax / elongationGridStep)
    % Is flame still supposed to move to that direction?

```

```

% If so, perform move. Else recalculate flameMove and move.
if g < (elongationPerTrip / elongationGridStep)
    flamePositionVsElongation(currentElongationStep + 2) ...
        = flamePositionVsElongation(currentElongationStep + 1) ...
        + flameMove * elongationGridStep / zStep;
    g = g + 1;
else
    if (abs(flamePositionVsElongation(currentElongationStep + 1) ...
        - lowerFlameLimitArrayElongation( ...
            currentElongationStep + 1))) ...
        < abs((flamePositionVsElongation( ...
            currentElongationStep + 1) ...
            - upperFlameLimitArrayElongation( ...
                currentElongationStep + 1))) % Flame at lower limit
        flameMove = ((upperFlameLimitArrayElongation( ...
            currentElongationStep + 1 + elongationPerTrip ...
            / elongationGridStep)) - ...
            lowerFlameLimitArrayElongation( ...
                currentElongationStep + 1)) / (elongationPerTrip / ...
                elongationGridStep);
    else % Flame at upper limit
        flameMove = -((upperFlameLimitArrayElongation( ...
            currentElongationStep + 1) - ...
            lowerFlameLimitArrayElongation( ...
                currentElongationStep + 1 + elongationPerTrip ...
                / elongationGridStep))) / (elongationPerTrip ...
                / elongationGridStep);
    end;
    flamePositionVsElongation(currentElongationStep + 2) ...
        = flamePositionVsElongation(currentElongationStep + 1) ...
        + flameMove * elongationGridStep / zStep;
    g = 1;
end;
% Then comes next step of elongation:
currentElongationStep = currentElongationStep + 1;
end;

% Plot result:
figure(2)
plot(elongationGrid, flamePositionVsElongation * zStep);
title('Flame brushing oscillation');
ylabel('Flame position [um]');
xlabel('Fiber elongation during pulling [um]');

```

Calculation of movement commands

The turning points of the brushing motion are transformed into *PVT* (position, velocity, time) commands for the control software *Motion Composer* of the *Aerotech* translation stages. The resulting output file can be copied to the controller to run the motion commands for the flame brushing.

```
tripCounter = 0;
currentElongationStep = 2;
accumulatedElongation = 0;
% For as long as desired elongation is reached:
while (currentElongationStep <= elongationMax / elongationGridStep)
    % If fiber is still to be pulled calculate next step of movement
    if mod(currentElongationStep, elongationPerTrip / ...
        elongationGridStep) == 0 % turning point is reached
        % Prepare the PVT command
        % One more full trip has been completed
        tripCounter = tripCounter + 1; % one more full trip has been made
        tripData(tripCounter).tripDuration ...
            = timePerMicronElongation * (currentElongationStep ...
                * elongationGridStep - accumulatedElongation);
        burnerTravelThisTrip = flamePositionVsElongation( ...
            currentElongationStep + 1) - flamePositionVsElongation( ...
                currentElongationStep - elongationPerTrip / ...
                    elongationGridStep + 1);
        tripData(tripCounter).leftStageMove = burnerTravelThisTrip ...
            - 0.5 * elongationPerTrip;
        tripData(tripCounter).rightStageMove = burnerTravelThisTrip ...
            + 0.5 * elongationPerTrip;
        accumulatedElongation = currentElongationStep ...
            * elongationGridStep;
        tripData(tripCounter).accumulatedElongation ...
            = accumulatedElongation;
    end;
    % Next step of elongation
    currentElongationStep = currentElongationStep + 1;
end;
% Calculate total pulling time:
totalPullingTime = sum([tripData(:).tripDuration]);
fprintf('\nTotal pulling time: %g s\n', totalPullingTime)

% Output file with movement commands for translation stages
filename = 'trajectory.ab'; % file extention 'ab' for 'aerobasic'

% Write trajectory file using the MOVEINC AeroBasic commands.
% d is the handle of the diameter-definition function
```

```

f = fopen(filename, 'w'); % open file for writing

% First line of file could include parameters as
% a comment (comment for Aerotech begins with ' )
timestamp = datestr(now, 31);
fprintf(f, '''Generated at %s\n', timestamp);
fprintf(f, '''Taper function: %s\n\n', func2str(d));

fprintf(f, 'ENABLE ZL ZR B\n'); % Make sure stages are enabled
fprintf(f, 'RAMP MODE RATE\n'); % Set the rate mode to RATE
fprintf(f, 'RAMP RATE 5\n'); % Specify the rate
fprintf(f, 'ABS\n'); % Set LINEAR mode to ABS moves
fprintf(f, 'LINEAR ZL 0 ZR 0 F 5\n'); % Move stages to initial position
fprintf(f, 'INC\n'); % Set mode to INC
% Move fiber a little back and forth so that in the video one can see
% when the sequence starts:
fprintf(f, 'LINEAR ZL 0.1 ZR 0.1 F 0.5\n');
fprintf(f, 'LINEAR ZL -0.1 ZR -0.1 F 0.5\n');
fprintf(f, 'ABS\n'); % Set mode to abs for burner position under fiber
fprintf(f, 'LINEAR B 48 F 2.5\n'); % move burner under fiber.
fprintf(f, 'DWELL 2\n'); % dwell 2 s under fiber before pulling.
fprintf(f, 'INC\n'); % Set mode to INC moves for the following PVT

fprintf(f, 'VELOCITY ON\n');

% Write data from tripData to file including the required commands
numberOfPoints = numel(tripData);
for i = 1: numberOfPoints % first column from tripData is not needed
    time = tripData(i).tripDuration;
    posLeftStage = tripData(i).leftStageMove / 1000; % from microns to mm
    posRightStage = tripData(i).rightStageMove / 1000; % from microns to mm
    vLeftStage = 0;
    vRightStage = 0;

    fprintf(f, 'PVT ZL %011.7f, %011.7f ZR %011.7f, %011.7f TIME %011.7f\n', ...
        posLeftStage, vLeftStage, posRightStage, vRightStage, time);
    if i == numberOfPoints - 1
        fprintf(f, 'VELOCITY OFF\n');
    end
end

% Remove burner
fprintf(f, 'ABS\n'); %
fprintf(f, 'DWELL 1\n'); %
fprintf(f, 'LINEAR B 5 F 2.5\n'); %

```

```
fclose(f);
```

A.3. Control software for mbed microcontroller

This is the shortened source code, that is executed on the mbed microcontroller of the electronics box, to have the outputs under computer control via an emulated terminal, e.g. with the software Tera Term.

```
// Pins to be controlled: 12-14, 21-30
// and 5-8 for SPI to DA-converter

#include "mbed.h"
#include "stdlib.h"

// Digital to analog converter via SPI with the pins 5 to 8.
SPI spi(p5, NC, p7); // mosi, NO miso used, sclk
DigitalOut sync(p6); // used as sync
DigitalOut refresh(p8); // used as refresh (LDAC)

// For communication with computer
Serial pc(USBTX, USBRX); // tx, rx

// Digital pins to be controlled:
DigitalOut ledGasFlowHydrogen(p12);
DigitalOut ledGasFlowOxygen(p13);
DigitalOut ledGasFlowProblem(p14);
DigitalOut flowbox(p21); // Switches flowbox on or off
DigitalOut light(p22); // Switches light on or off
DigitalOut aux(p23); // Switches auxiliary output on or off
DigitalOut ignitionWireEnable(p24); // Enables ignition wire
PwmOut ignitionWireSSR(p25); // Switches on or off ignition wire
DigitalOut output24V(p26); // Switches on or off 24 V output
DigitalOut outputFiberIllumination(p27); // Switches on or off LEDs
DigitalOut output5V(p28); // Switches on or off 5 V output
DigitalOut outputGasFlowSupply(p29); // Switches on or off 24 V
DigitalOut ledStagesError(p30); // LED to indicate error

int main()
{

// Initial values for all outputs:
ledGasFlowHydrogen = 0; // 0 = off
ledGasFlowOxygen = 0;
```

```

ledGasFlowProblem = 0;
flowbox = 1; // 1 = on (via relais which determines initial position)
light = 1; // 1 = off (via relais which defines initial position)
aux = 1; // 1 = off (via relais which defines initial position)
ignitionWireEnable = 1; // 1 = off
ignitionWireSSR = 1; // 1 = off
// Set periode for pulse width modulation to 50ms
ignitionWireSSR.period_ms(50);
output24V = 1; // 1 = off
output5V = 1; // 1 = off
outputFiberIllumination = 1; // 1 = off
outputGasFlowSupply = 1; // 1 = off
ledStagesError = 0; // 0 = off

//For gas flow:
// Setup the SPI for 8 bit data, high steady state clock, second edge
// capture (needed for this DA-conv.), with a 100kHz clock rate
spi.format(8,2);
spi.frequency(100000);
refresh = 0; // Sets output of DA-conv. whenever sync is high

// Initializing the output range to 0..10V (handbook page 25)
sync = 0; // Start writing to DAC by setting sync to low
wait_us(40); // Gap for safety
// Send the command:
spi.write(12); // Send 00001100
spi.write(0); // Send 00000000
spi.write(1); // Send 00000001
wait_us(40); // Gap for safety
sync = 1; // Stop writing to DAC by setting sync to high
wait_us(80);

// Power up the two outputs (handbook page 26)
sync = 0; // Start writing to DAC by setting sync to low
wait_us(40); // Gap for safety
// Send the command:
spi.write(16); // Send 00010000
spi.write(0); // Send 00000000
spi.write(5); // Send 00000101
wait_us(40); // Gap for safety
sync = 1; // Stop writing to DAC by setting sync to high
wait_us(80);

// Syntax of trigger comamnds:
// First part specifies the device, second part is value
char command_type; // First part

```

```

float target_value = 0; // Second part, e.g. 0 or 1 or gas flow value

int target_value_int = 0; // Target value for digital outputs
int validComand = 0; // Is set to 1 if a valid comand is evaluated
float target_value_new_range = 0; // This is to calculate the scaled
//(0...65536) target value for the DA-converter
int binary[16]; // To save result of conversion to binary
int little_helper = 0;
int i = 0; // First 8 bits to be Send via SPI
int ii = 0; // Second 8 bits to be Send via SPI
int iii = 0; // Third 8 bits to be Send via SPI

start: // for jump

pc.printf("Available digital commands are\n\r
ledGasFlowHydrogen: a\n\r
ledGasFlowOxygen: p\n\r
ledGasFlowProblem: c\n\r
flowbox: d\n\r
light: e\n\r
aux: f\n\r
ignitionWireEnable: g\n\r
ignitionWireSSR: n\n\r
output24V: i\n\r
outputFiberIllumination: k\n\r
output5V: j\n\r
outputGasFlowSupply: l\n\r
ledStagesError: m\n\r
each followed by either 0 or 1, e.g. type a1 + enter.\n\r
For the gas flow type h (hydrogen) or o (oxygen) or b (both)
followed by a (real) number >= 0 and <= 100 without space and enter.

while(1) {
    //gasFlowHydrogen
    if (command_type == 'h') {
        if ((target_value < 0) || (target_value > 100)) {
            pc.printf ("\nTarget value for gas flow
                        must be between 0 and 100!!!\n\r");
            goto start; //jump
        } //if
        validComand = 1;
        // calculate ii and iii from target value (binary number)
        target_value_new_range = ceil( ...
        target_value * 65535 * 0.01); //rescaling the target value
        for (int counter = 0, helper = target_value_new_range; ...
        counter <=15; counter++) {

```

```

binary[counter] = helper % 2;
little_helper >>=1;
    } //for
iii = 128 * binary[7] + 64 * binary[6] ...
      + 32 * binary[5] + 16 * binary[4] ...
      + 8 * binary[3] + 4 * binary[2] ...
      + 2 * binary[1] + 1 * binary[0];
ii = 128 * binary[15] + 64 * binary[14] ...
     + 32 * binary[13] + 16 * binary[12] ...
     + 8 * binary[11] + 4 * binary[10] ...
     + 2 * binary[9] + 1 * binary[8];
i = 0; // So that the output is channel A to hydrogen
sync = 0; // Start writing to DAC by setting sync to low
wait_us(40); // Gap for safety
// Send the command:
spi.write(i); // Send first 8 bits
spi.write(ii); // Send second 8 bits (data)
spi.write(iii); // Send third 8 bits (data)
wait_us(40); // Gap for safety
sync = 1; // Stop writing to DAC by setting sync to high
wait_us(80);
pc.printf("now gasflow %c = %f.\n\r", ...
command_type, target_value);
} // if

```

(truncated: same for oxygen)

(truncated: same for both gases at once)

```

//ledGasFlowHydrogen
if (command_type == 'a') {
    target_value_int = ceil(target_value);
    if ((abs(target_value_int - target_value)) < 0.1) {
        validComand = 1;
    } // if
    ledGasFlowHydrogen = target_value_int;
    pc.printf("now ledGasFlowHydrogen = %i.\n\r", ...
        target_value_int);
} // if

```

(truncated: same for output ledGasFlowOxygen)

(truncated: same for output ledGasFlowProblem)

(truncated: same for output flowbox)

(truncated: same for output light)

(truncated: same for output aux)

(truncated: same for output output24V)

```

(truncated: same for output output5V)
(truncated: same for output outputFiberIllumination)
(truncated: same for output outputGasFlowSupply)
(truncated: same for output ledStagesError)
(truncated: same for output ignitionWireEnable)

    //ignitionWireSSR
    if (command_type == 'n') {
        target_value_int = ceil(target_value);
        if ((abs(target_value_int - target_value)) < 0.1) {
            validComand = 1;
        } // if
        if (target_value_int == 1) {
            ignitionWireSSR = target_value_int;
            pc.printf("now ignitionWireSSR = off.\n\r");
        } //if
        else {
            ignitionWireSSR = 0;
            wait(1);
            ignitionWireSSR = 0.8; // 80 percent duty cycle
            pc.printf("now ignitionWireSSR = on.\n\r");
        }
    } // if

    // invalid comand
    if (validComand == 0) {
        pc.printf("Invalid comand: '%c%f'.\n\r", ...
            command_type, target_value);
    } // if

    validComand = 0;

    } // if readable
} //while
} //main

```


B. Parameters of the presented OMFs

This is a compilation of the fabrication parameters for the OMFs that are analyzed in chapter 5. For reference, for each OMF the internal identification number is given, too.

Table B.1. Fabrication parameters of the OMFs discussed in this thesis.

OMF sample	Internal number	D_w [μm]	L_w [mm]	Ω [mrad]	Number of brushing trips	Time per micron elongation [s]	Gas flow rate H_2+O_2 [ml/min]	Fiber type
OMF for transmittance	243	0.5	5	1.5	86	0.018	86 + 44	SM800
sample one	240	20	10	3.0	38	0.008	86 + 44	SMF-28
sample two	238	40	10	3.0, $D > 71 \mu\text{m}$ 1.5, $D < 71 \mu\text{m}$	40	0.01	86 + 44	SMF-28
sample three	242	10	20	3.0	44	0.008	86 + 44	SMF-28
sample four	237	40	5	1.5	56	0.02	86 + 44	SMF-28

Bibliography

- [1] B. Sartorius, H. Roehle, H. Künzel, J. Böttcher, M. Schlak, D. Stanze, H. Venghaus, and M. Schell, “All-fiber terahertz time-domain spectrometer operating at 1.5 μm telecom wavelengths,” *Optics Express*, vol. 16, p. 9565, June 2008.
- [2] J. Senior, *Optical Fiber Communications: Principles and Practice*. Harlow, England: Prentice Hall, 3 ed., 2008.
- [3] G. J. Tearney, M. E. Brezinski, B. E. Bouma, S. A. Boppart, C. Pitris, J. F. Southern, and J. G. Fujimoto, “In vivo endoscopic optical biopsy with optical coherence tomography,” *Science (New York, N.Y.)*, vol. 276, pp. 2037–9, June 1997.
- [4] C. Chow, F. M. Kuo, J. W. Shi, C. H. Yeh, Y. F. Wu, C. H. Wang, Y. T. Li, and C. L. Pan, “100 GHz ultra-wideband (UWB) fiber-to-the-antenna (FTTA) system for in-building and in-home networks,” *Optics Express*, vol. 18, p. 473, Jan. 2010.
- [5] M. Sumetsky, “How thin can a microfiber be and still guide light?,” *Optics letters*, vol. 31, pp. 870–2, Apr. 2006.
- [6] R. Garcia-Fernandez, W. Alt, F. Bruse, C. Dan, K. Karapetyan, O. Rehband, A. Stiebeiner, U. Wiedemann, D. Meschede, and A. Rauschenbeutel, “Optical nanofibers and spectroscopy,” *Appl. Phys. B*, vol. 105, p. 13, May 2011.
- [7] D. A. Akimov, A. A. Ivanov, A. N. Naumov, O. A. Kolevatova, M. V. Alfimov, T. A. Birks, W. J. Wadsworth, P. S. J. Russell, A. A. Podshivalov, and A. M. Zheltikov, “Generation of a spectrally asymmetric third harmonic with unamplified 30-fs Cr: forsterite laser pulses in a tapered fiber,” *Applied Physics B: Lasers and Optics*, vol. 76, no. 5, pp. 515–519, 2003.
- [8] T. Wang, X. Li, F. Liu, W. Long, Z. Zhang, L. Tong, and Y. Su, “Enhanced fast light in microfiber ring resonator with a Sagnac loop reflector.,” *Optics express*, vol. 18, pp. 16156–61, July 2010.
- [9] J. E. Hartung, *Surface protection of optical microfibres for caesium spectroscopy*. Diploma thesis, U. Bonn, 2012.
- [10] U. Wiedemann, K. Karapetyan, C. Dan, D. Pritzkau, W. Alt, S. Irsen, and D. Meschede, “Measurement of submicrometre diameters of tapered optical fibres using harmonic generation,” *Optics Express*, vol. 18, p. 7693, Mar. 2010.
- [11] K. Karapetyan, *Single optical modal interferometer*. PhD thesis, U. Bonn, 2012.

- [12] A. Rauschenbeutel, "Trapping and Interfacing Cold Neutral Atoms Using Optical Nanofibers," in *Q36.2 DPG-Conference, Stuttgart*, 2012.
- [13] F. Warken, *Ultradünne Glasfasern als Werkzeug zur Kopplung von Licht und Materie*. PhD thesis, U. Bonn, 2007.
- [14] A. Stiebeiner, R. Garcia-Fernandez, and A. Rauschenbeutel, "Design and optimization of broadband tapered optical fibers with a nanofiber waist.," *Optics express*, vol. 18, pp. 22677–85, Oct. 2010.
- [15] U. Wiedemann, *Control of photochromic molecules adsorbed to optical microfibres*. PhD thesis, U. Bonn, 2011.
- [16] T. A. Birks and Y. W. Li, "The shape of fiber tapers," *Journal of Lightwave Technology*, vol. 10, pp. 432–438, Apr. 1992.
- [17] J. D. Love, W. M. Henry, W. J. Stewart, R. J. Black, S. Lacroix, and F. Gonthier, "Tapered single-mode fibres and devices," *Proc. Inst. Elect. Eng.*, vol. 138, no. 5, pp. 343–354, 1991.
- [18] F. Warken, E. Vetsch, D. Meschede, M. Sokolowski, and A. Rauschenbeutel, "Ultra-sensitive surface absorption spectroscopy using sub-wavelength diameter optical fibers," *Opt. Express*, vol. 15, no. 19, pp. 11952–11958, 2007.
- [19] G. Brambilla, "Optical fibre nanowires and microwires: a review," *Journal of Optics*, vol. 12, p. 043001, Apr. 2010.
- [20] S. Pricking and H. Giessen, "Tapering fibers with complex shape.," *Optics express*, vol. 18, pp. 3426–37, Feb. 2010.
- [21] A. F. Holleman, E. Wiberg, and N. Wiberg, *Lehrbuch der Anorganischen Chemie*. Berlin: Walter de Gruyter & Co, 102 ed., 2007.
- [22] L. P. Davila, S. H. Risbud, and J. F. Shackelford, *Ceramic and Glass Materials*. Berlin: Springer, 2008.
- [23] M. Kocifaj and J. Majling, "Light scattering simulations relevant to crystallization of lithiumdisilicate glass," *Journal of Non-Crystalline Solids*, vol. 357, pp. 1452–1454, Mar. 2011.
- [24] A. K. Varshneya, *Fundamentals of Inorganic Glasses*. San Diego: Academic Press, 1993.
- [25] Aerotech Inc., "ANT130-L Series," 2012.
- [26] F. Warken, A. Rauschenbeutel, and T. Bartholomäus, "Fiber Pulling Profits from Precise Positioning," *Photonics Spectra*, vol. 42, no. 3, p. 73, 2008.
- [27] I. Glassman and R. Yetter, *Combustion*. London: Elsevier, 4 ed., 2008.
- [28] F. Joos, *Technische Verbrennung, Verbrennungstechnik, Verbrennungsmodellierung, Emissionen*. Berlin: Springer, 2006.

- [29] GoodFellow Cambridge Ltd., “Material properties – Alloy – Electrical properties,” 2011.
- [30] K. Karapetyan, *private communication*. 2011.
- [31] D. Tritton, *Physical Fluid Dynamics*. Oxford: Oxford University Press, USA, 2 ed., 1988.
- [32] Bronkhorst Maettig GmbH, “Mass-Flow Select,” 2011.
- [33] Mitutoyo U.S.A., “Objectives Series 378 – Specifications,” 2012.
- [34] Fibercore Ltd., “Singlemode Optical Fiber,” 2012.
- [35] M. Sumetsky, “How thin can a microfiber be and still guide light? Errata,” *Optics Letters*, vol. 31, p. 3577, Sept. 2006.
- [36] D. Pritzkau, *Measurement of submicrometer diameters of tapered optical fibres using scanning electron microscopy*. Diploma thesis, U. Bonn, 2010.
- [37] D. J. Butler and G. W. Forbes, “Fiber-diameter measurement by occlusion of a Gaussian beam,” *Applied Optics*, vol. 37, no. 13, 1998.
- [38] F. Warken and H. Giessen, “Fast profile measurement of micrometer-sized tapered fibers with better than 50-nm accuracy,” *Optics letters*, vol. 29, pp. 1727–9, Aug. 2004.
- [39] Mitutoyo America Corp., “Digimatic Micrometer Series 293 MDC-Lite,” 2012.
- [40] Corning Inc., “Corning SMF-28 ULL Optical Fiber,” 2011.
- [41] H. Konishi, H. Fujiwara, S. Takeuchi, and K. Sasaki, “Polarization-discriminated spectra of a fiber-microsphere system,” *Applied Physics Letters*, vol. 89, no. 12, p. 121107, 2006.
- [42] L. Ding, C. Belacel, S. Ducci, G. Leo, and I. Favero, “Ultralow loss single-mode silica tapers manufactured by a microheater,” *Applied Optics*, vol. 49, p. 2441, Apr. 2010.
- [43] M. Spurny, *private communication*. 2012.

Acknowledgements / Danksagung

Mein primärer Dank gilt Herrn Meschede für die Vergabe einer Master-Arbeit, deren Schwerpunkt so genau meinem gewünschten Tätigkeitsfeld entsprach. Insbesondere danke ich für das große Vertrauen, das er dabei in mich setzte. Ebenso möchte ich Herrn Linden danken, dass er das zweite Gutachten zu meiner Arbeit anfertigt.

Allen Mitgliedern des Faser-Teams danke ich für ihren Erfahrungsschatz, den sie mit mir teilten, für ihre stets willkommenen und hilfreichen Ratschläge. Namentlich möchte ich hier Marcel, Wolfgang, Konstantin und Jan nennen. Sie leiteten mich stets zielführend an, hielten für mich Lösungsansätze bereit und begleiteten mich bei technischen Fragen zur Machbarkeit und Umsetzung. Außerdem haben sie durch unmittelbare Mithilfe an kritischen Stellen den Fortschritt erheblich beschleunigt. Der gesamten Arbeitsgruppe gilt mein Dank für die sehr angenehme Arbeitsatmosphäre.

Darüber hinaus danke ich den Feinmechanik- und Elektronik-Werkstätten, die das Unmögliche mehr als einmal möglich gemacht haben. Ein besonderes Dank geht dabei an Herrn Langen und Herrn Brähler für ihre Beratungen in verschiedenen Stadien dieser Arbeit, Herrn Frenzel für die Einweisungen in der Studentenwerkstatt und Herrn Korte für die Installation des Gaswarnsystems. Der gesamten Verwaltung des IAP möchte ich für die reibungslose Abwicklung aller organisatorischen Abläufe danken und für die – vermutlich – einhundert Benachrichtigungen für eingetroffene Warenlieferungen. Ein besonderer Dank sei an Dietmar gerichtet, der mehrfach mit seinen Kontakten und Kenntnissen über die Gebäudetechnik des IAP zeitliche Abläufe massiv verkürzen konnte.

Ein herzliches Dankeschön gilt zuletzt auch meinen Eltern und Martina, dafür dass sie mich im gesamten Verlauf meines Studiums auf so vielfältige Arten unterstützt haben und ich stets auf ihren Rückhalt bauen konnte.

I hereby certify that the work presented here was accomplished by myself and without the use of illegitimate means or support, and that no sources and tools were used other than those cited.